Geophys. J. Int. (2005) **161,** 763–788 doi: 10.1111/j.1365-246X.2005.02592.x

Seismic structure of the Carnegie ridge and the nature of the Galápagos hotspot

Valentí Sallarès[1,*] Philippe Charvis,[1] Ernst R. Flueh,[2] Joerg Bialas[2] and the SALIERI Scientific Party†

[1] *IRD-Géosciences Azur, B.P. 48,* 06235 *Villefranche-sur-Mer, France. E-mail: valenti.sallares@obs-vlfr.fr*
[2] *IFM-GEOMAR, Leibniz Institut for Marine Sciences, Kiel and* SFB574 *of CAU, Kiel,* 1-3 *Wischhofstrasse,* 24148 *Kiel, Germany*

Accepted 2005 January 24. Received 2004 November 22; in original form 2004 January 19

SUMMARY

The Galápagos volcanic province (GVP) includes several aseismic ridges resulting from the interaction between the Galápagos hotspot (GHS) and the Cocos–Nazca spreading centre (CNSC). The most prominent are the Cocos, Carnegie and Malpelo ridges. In this work, we investigate the seismic structure of the Carnegie ridge along two profiles acquired during the South American Lithospheric Transects Across Volcanic Ridges (SALIERI) 2001 experiment. Maximum crustal thickness is ∼19 km in the central Carnegie profile, located at ∼85°W over a 19–20 Myr old oceanic crust, and only ∼13 km in the eastern Carnegie profile, located at ∼82°W over a 11–12 Myr old oceanic crust. The crustal velocity models are subsequently compared with those obtained in a previous work along three other profiles over the Cocos and Malpelo ridges, two of which are located at the conjugate positions of the Carnegie ones. Oceanic layer 2 thickness is quite uniform along the five profiles regardless of the total crustal thickness variations, hence crustal thickening is mainly accommodated by layer 3. Lower crustal velocities are systematically lower where the crust is thicker, thus contrary to what would be expected from melting of a hotter than normal mantle. The velocity-derived crustal density models account for the gravity and depth anomalies considering uniform and normal mantle densities (3300 kg m^{-3}), which confirms that velocity models are consistent with gravity and topography data, and indicates that the ridges are isostatically compensated at the base of the crust. Finally, a two-dimensional (2-D) steady-state mantle melting model is developed and used to illustrate that the crust of the ridges does not seem to be the product of anomalous mantle temperatures, even if hydrous melting coupled with vigorous subsolidus upwelling is considered in the model. In contrast, we show that upwelling of a normal temperature but fertile mantle source that may result from recycling of oceanic crust prior to melting, accounts more easily for the estimated seismic structure as well as for isotopic, trace element and major element patterns of the GVP basalts.

Key words: aseismic ridge, Galápagos hotspot, gravity, mantle melting, seismic tomography.

1 INTRODUCTION

The origin of large igneous provinces and aseismic ridges is usually associated with the presence of hot mantle plumes rising from the deep mantle, whose surface imprint is referred to as hotspot (Wilson 1963; Morgan 1971). The thermal plume model asserts that a hot, rising plume enhances mantle melting and that the excess of melting is mostly emplaced as igneous crust (McKenzie & Bickle 1988; White & McKenzie 1989, 1995). The primary support for this hypothesis is the thick crust of both aseismic ridges and igneous provinces as compared with normal oceanic crust (e.g. Coffin & Eldholm 1994; Charvis *et al.* 1995; Darbyshire *et al.* 2000; Charvis & Operto 1999; Grevemeyer *et al.* 2001; Sallarès *et al.* 2003). The crustal overthickening is reflected in the prominent topography and gravity anomalies that characterize these structures (Anderson *et al.* 1973; Cochran & Talwani 1977). Additional arguments repeatedly invoked to support the thermal plume model include:

*Now at: Unitat de Tecnologia Marina—CMIMA—CSIC Passeig Marítim de la Barceloneta 37-49, 08003 Barcelona, Spain. E-mail: vsallares@utm.csic.es
†The SALIERI Scientific Party: W. Agudelo, A. Anglade, A. Berhorst, N. Bethoux, A. Broser, A. Calahorrano, J.-Y. Collot, N. Fekete, A. Gailler, M. A. Gutscher, Y. Hello, P. Liersch, F. Michaud, M. Müller, J. A. Osorio, C. Ravaut, K. P. Steffen, P. Thierer, C. Walther, B. Yates.

(i) the composition of the hotspot basalts, which generally exhibit a distinct geochemical signature from the mid-ocean ridge basalts (MORB) and is in agreement with that expected for melting of a hotter than normal mantle (Watson & McKenzie 1991; White *et al.* 1992);

(ii) the high-velocity crustal roots frequently found in oceanic plateaus, aseismic ridges and passive volcanic margins (e.g. Coffin & Eldholm 1994; Kelemen & Holbrook 1995; Grevemeyer *et al.* 2001); and

(iii) the mantle low-velocity anomalies extending from the surface to the lower mantle shown by global tomography models, particularly in Iceland (Bijwaard & Spakman 1999; Ritsema & Allen 2003).

Regardless of the wide acceptance of the thermal plume model, several alternatives have been also proposed. The small-scale convection model shows that systems cooled from above having lateral temperature contrasts will develop small-scale convection up to an order of magnitude faster than plate motions (e.g. Korenaga & Jordan 2002). In addition, it has been demonstrated that rifting may induce dynamic convection within the mantle as well (Boutilier & Keen 1999). The rapid vertical convection will increase melt production in the upper mantle without the necessity of having hot mantle plumes. It has also been proposed that mantle plumes may include a significant proportion of lower melting components, such as eclogite derived from recycled oceanic crust (Cordery *et al.* 1997; Campbell 1998). The importance of major element source heterogeneity to account for the excess of melting has been also proposed for a number of hotspots including Hawaii (Hauri 1996), Açores (Schilling *et al.* 1983) and Iceland (Korenaga & Kelemen 2000). It has been also suggested that some so-called hotspots are actually wet-spots of normal temperature (e.g. Açores), based on the composition of the abyssal peridotites (Bonatti 1990). Last but not least, recent seismic experiments show that high-velocity crustal roots are absent in the Greenland margin (North Atlantic volcanic province) (Korenaga *et al.* 2000), and the Cocos and Malpelo ridges (Galápagos volcanic province, GVP; Sallarès *et al.* 2003), and none of the local tomography studies yet performed in Iceland shows compelling evidence of a velocity anomaly extending deeper than the mantle transition zone (e.g. Foulger *et al.* 2001; Wolfe *et al.* 2002).

The GVP constitutes a well-studied example of an igneous province generated by the interaction between the Galápagos hotspot (GHS) and the Cocos–Nazca spreading centre (CNSC). Different geophysical studies based mainly on gravity analysis, seismic data and numerical models along the present and palaeo-axes of the CNSC suggest that the GHS is a thermal anomaly (Schilling 1991; Ito & Lin 1995; Ito *et al.* 1997; Canales *et al.* 2002), and the receiver function analysis claims that the associated mantle plume extends deeper than the mantle transition zone (Hooft *et al.* 2003). However, recent seismic modelling along three wide-angle profiles acquired during the Panama basin and Galápagos plume-New Investigations of Intra plate magmatism (PAGANINI-1999) experiment have shown that the velocity and density structure of Cocos and Malpelo aseismic ridges (Fig. 1) is not consistent with that expected for a crust generated by decompression melting of a hot mantle plume (Sallarès *et al.* 2003). In addition, available global tomography models do not show any Galápagos-linked anomaly going deeper than the base of the upper mantle (Courtillot *et al.* 2003; Ritsema & Allen 2003; Montelli *et al.* 2004). In this paper, we present additional velocity models from two new transects acquired across the Carnegie ridge during the South American Lithospheric Transects Across Volcanic Ridges (SALIERI) seismic experiment in 2001 (Flueh *et al.* 2001; Fig. 1). The velocity models are compared with those previously obtained in Cocos and Malpelo ridges. Then, the velocity-derived density models are used to determine the mantle density structure that best fits the gravity and topography anomalies. Finally, a two-dimensional (2-D) steady-state mantle melting model is developed and used to estimate the range of mantle melting parameters (potential temperature, deep upwelling ratio, presence of a hydrous root) that best explains the crustal structure of the aseismic ridges and thus to infer a possible nature for the GHS.

2 TECTONIC SETTING AND PREVIOUS WORK

The GVP is an excellent natural laboratory to investigate melting processes resulting from the interaction between a spreading centre and a melt anomaly. It constitutes several aseismic ridges, which have resulted from the interaction between the CNSC and the GHS during the last 20 Myr The most prominent are the Cocos, Carnegie and Malpelo ridges, which show the imprint of the GHS into the Cocos and Nazca plates (Fig. 1). Different works based on magnetic and bathymetric data suggest that seafloor spreading along the CNSC originated at ∼23 Ma, following a major plate reorganization, which broke the ancient Farallon Plate along a pre-existing fracture zone (e.g. Hey 1977; Lonsdale & Klitgord 1978; Barckhausen *et al.* 2001). At that time, the GHS was located near the CNSC, and had begun accreting both the Cocos and Carnegie ridges.

At present day, the GHS is located beneath the Galápagos archipelago, at ∼190 km south from the CNSC (Fig. 1). Recent Global Positioning System (GPS) measurements indicate that the Nazca Plate is moving approximately towards 90°NE at 58 ± 2 km Myr^{-1} and the Cocos Plate towards 41°NE at 83 ± 3 km Myr^{-1} with respect to the stable South American craton (Freymueller *et al.* 1993; Trenkamp *et al.* 2002). Those motions are basically the addition of ∼60 km Myr^{-1} seafloor spreading along the CNSC (Sallarès & Charvis 2003), E–W spreading along the East Pacific Rise (∼110 km Myr^{-1} at 2°N, based on DeMets *et al.* 1990) and ∼26 km Myr^{-1} northward migration of the CNSC in the GHS reference frame (Sallarès & Charvis 2003). The CNSC migration, together with the occurrence of ridge jumps along the spreading axis between 19.5 and 14.5 Ma, have resulted in significant variations in the relative location of the GHS and the CNSC during the last 20 Myr. Between 20 and ∼12 Ma, the GHS was approximately ridge-centred, between ∼12 and 7.5 Ma it was located beneath the Cocos Plate, and from then to now it has been located beneath the Nazca Plate (Barckhausen *et al.* 2001; Sallarès & Charvis 2003). The Panama fracture zone (PFZ), which is a major tectonic feature of the GVP, opened at ∼9 Ma, triggered by the cessation of the easternmost Cocos Plate subduction beneath Middle America. The strike-slip motion along the dextral PFZ lead to the separation between the Cocos and Malpelo ridges (Sallarès & Charvis 2003).

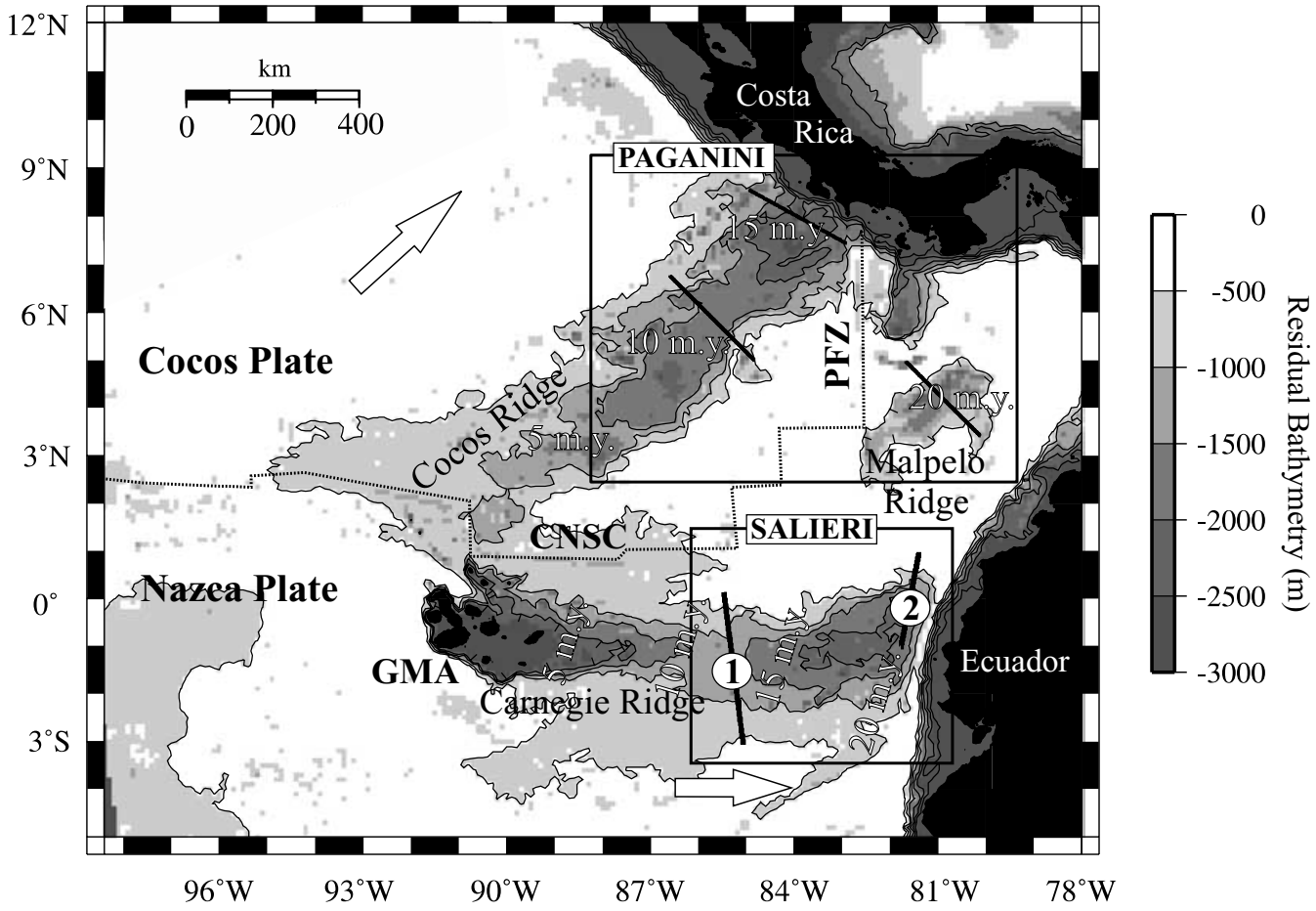

Figure 1. Location map of the study zone showing the residual bathymetry derived from the seafloor age (Mueller *et al.* 1996), based on the plate cooling model of Parsons & Sclater (1977) for ages smaller than 70 Myr ($d = 2500 + 350t^{1/2}$). Numbers show crustal ages of oceanic plates at 5 Ma intervals. Large arrows display plate motions relative to the stable South American craton (Trenkamp *et al.* 2002). Black lines show the location of all the wide-angle seismic profiles and numbers indicate the two profiles used in this work (profile 1, Western Carnegie; profile 2, Eastern Carnegie). Boxes outline the seismic experiments recently performed in Cocos, Malpelo and Carnegie (PAGANINI-1999; SALIERI-2001). CNSC, Cocos–Nazca Spreading Centre; GHS, Galápagos hotspot; PFZ, Panama fracture zone.

A large number of geophysical and geochemical studies have been performed in the GVP. These works include:

(i) geochemical analysis and dating of samples dredged along the present-day ridge axis and across the aseismic ridges (Schilling *et al.* 1982; Verma *et al.* 1983; Hoernle *et al.* 2000; Detrick *et al.* 2002);

(ii) gravity and topography analysis along the present and palaeo-axes of the CNSC (Schilling 1991; Ito & Lin 1995; Canales *et al.* 2002);

(iii) numerical modelling of the plume–ridge interaction (Ito *et al.* 1996, 1999);

(iv) identification and reconstruction of magnetic anomalies (Hey 1977; Lonsdale & Klitgord 1978; Hardy 1991; Wilson & Hey 1995; Barckhausen *et al.* 2001);

(v) receiver function analysis at the Galápagos platform (Hooft *et al.* 2003); and

(vi) wide-angle seismic models of the crustal structure across the Cocos and Malpelo ridges (Trummer *et al.* 2002; Walther 2002; Sallarès *et al.* 2003; Walther 2003), the Galápagos platform (Toomey *et al.* 2001) and the CNSC (Canales *et al.* 2002).

The results of these studies have been also used to infer the geodynamic evolution of the GVP (e.g. Hey 1977; Barckhausen *et al.* 2001; Sallarès & Charvis 2003) and to estimate the excess temperature associated with the presence of the GHS along the present ridge and palaeoridge axis of the CNSC (Schilling 1991; Ito & Lin 1995; Canales *et al.* 2002). A quantitative estimation of the influence of the distinct melting parameters on the crustal structure observed at the Cocos, Carnegie and Malpelo ridges, however, has been so far lacking.

3 WIDE-ANGLE DATA SET

The seismic data set used in this study constitutes 52 seismic sections recorded along two wide-angle profiles, which were acquired in the summer of 2001 during the SALIERI cruise aboard the German R/V Sonne. Shooting along both profiles was conducted using three 2000 cubic inch airguns and a firing interval of 60 s, with a shot spacing of around 120 m. The set of receivers constituted 24 Geomar ocean bottom hydrophones (OBH) and ocean bottom seismometers (OBS) together with 13 Institut de Recherche pour le Développement (IRD) OBS. The

Table 1. Values of the different parameters used in the seismic data processing.

Processing stage	Parameter	Value
Deconvolution	Operator length	0.3 s
	Prediction lag	0.01 s
	Noise level	0.001 per cent
	Length of autocorrelation window	20 s
Filtering	Frequency range	3–13 Hz
AGC	Length of time window	2 s

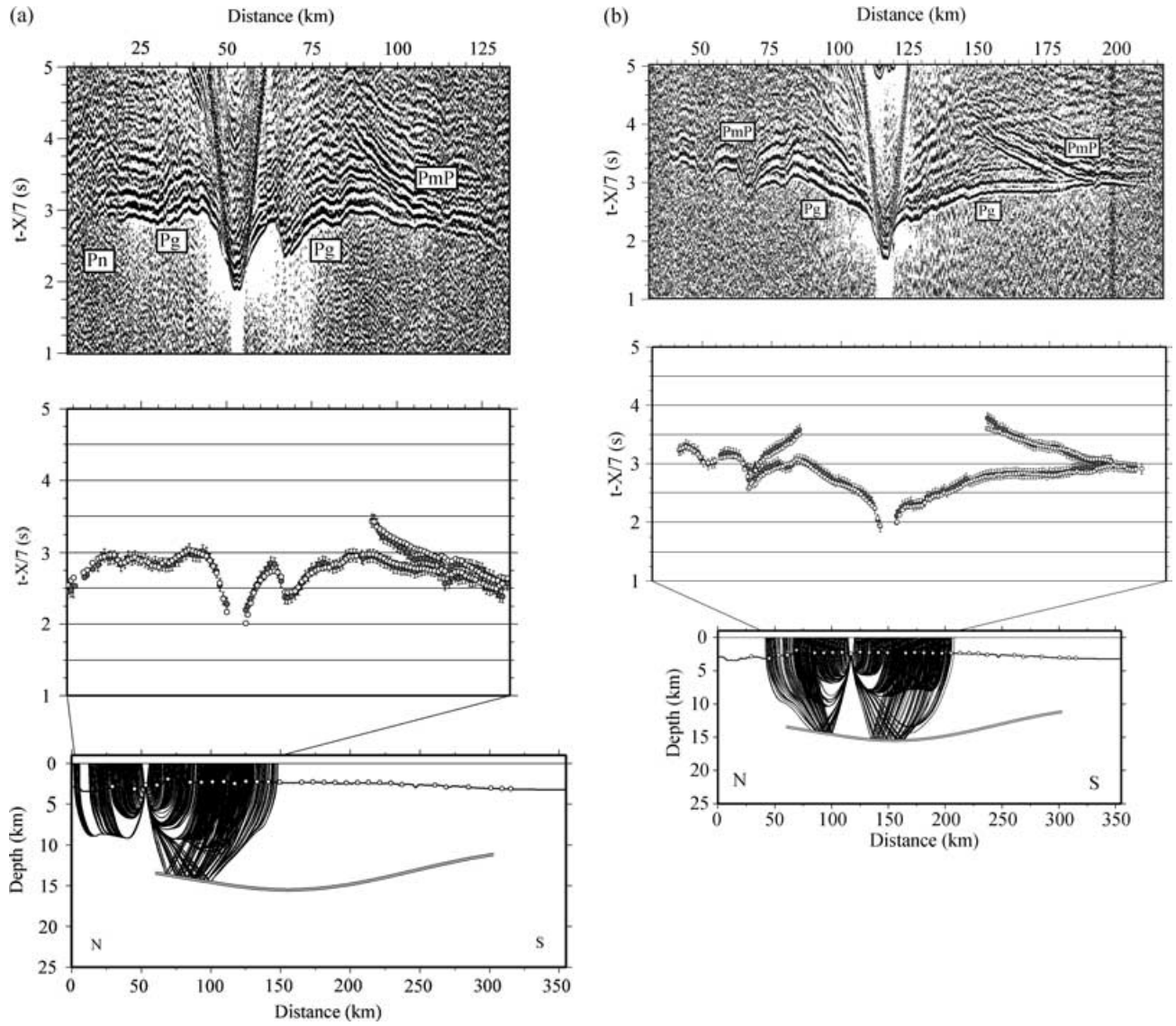

Figure 2. Seismic gathers recorded along the numbered profiles of Fig. 1. Systematic data processing consisting of 5–15 Hz butterworth filtering, predictive deconvolution and automatic gain correction was applied to all the gathers (top). Picked traveltimes (solid circles with error bars) and predicted traveltimes (open circles) for P_g and P_mP phases using the velocity models displayed in Fig. 3 (middle). Ray tracing corresponding to the same models (bottom). (a) Ocean bottom seismometers (OBS) 3, profile 1; (b) OBS 10, profile 1; (c) OBS 17, profile 1; (d) OBS 23, profile 1; (e) OBS 29, profile 1; (f) OBS 5, profile 2; (g) OBS 10, profile 2; (h) OBS 13, profile 2; (i) OBS 19, profile 2.

first profile (profile 1 in Fig. 1) includes 30 OBS and OBH that were deployed along a 350 km N–S trending transect, which crosses the saddle of the Carnegie ridge at ∼85°W. The receiver spacing along this line was between 7 and 15 km. The second profile (profile 2 in Fig. 1), comprises 22 instruments deployed along a N–S transect of 230 km covering the northern flank of the ridge near the subduction zone, at ∼82°W. Receiver spacing was similar to that of profile 1. The location of both seismic lines and those of three other transects acquired across the Cocos and Malpelo ridges during the PAGANINI-1999 experiment are shown in Fig. 1.

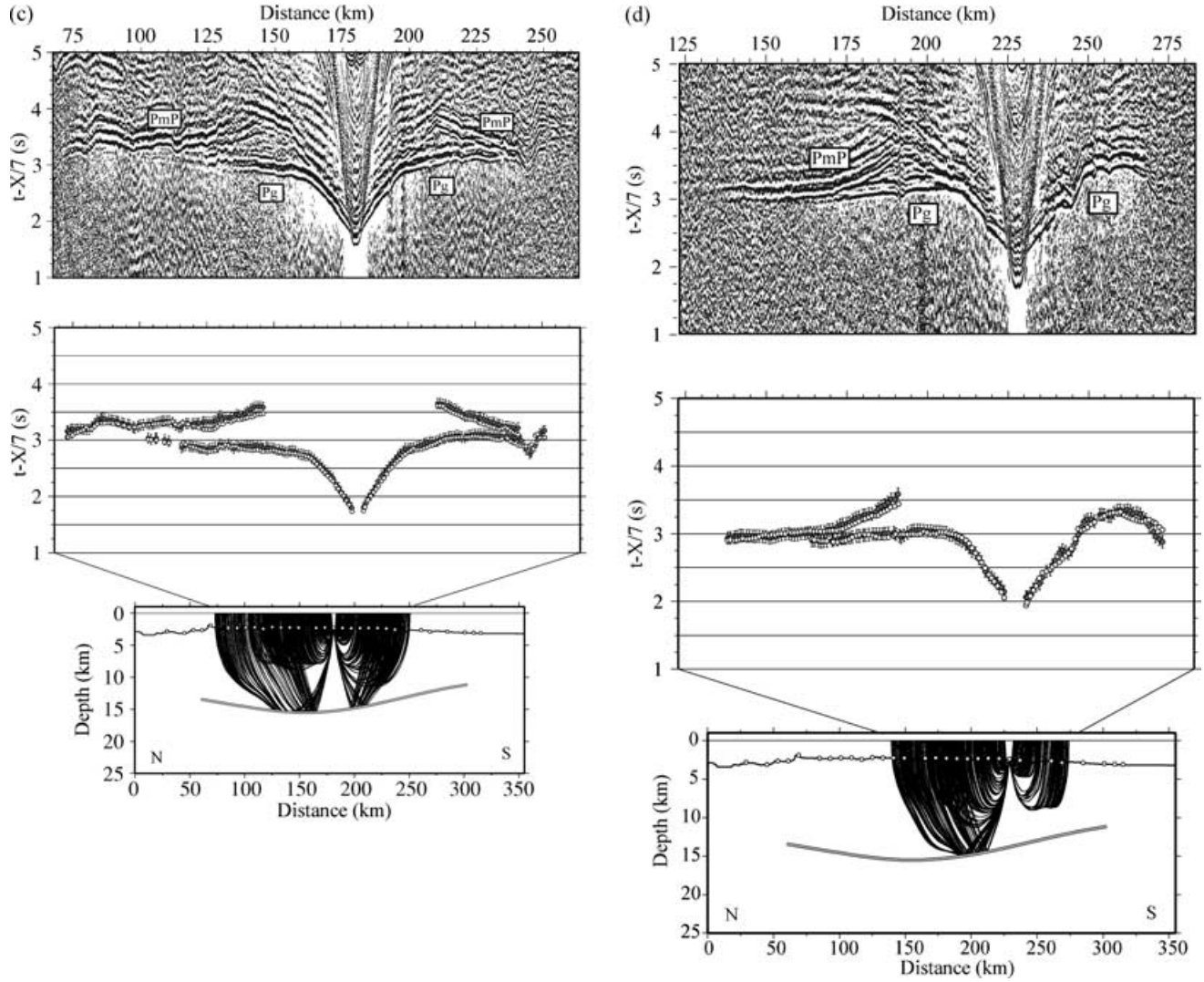

Figure 2. (*Continued.*)

The data acquired along both profiles have a very good quality. Systematic data processing consisting of time and distance depending predictive deconvolution and frequency filtering, and automatic gain control was applied to the recorded seismic gathers (see parameters in Table 1). Several of the record sections are shown in Fig. 2. The seismic phases observed in all record sections are predominantly first arrivals corresponding to waves refracted within the oceanic crust (P_g) and clear secondary arrivals identified as reflections in the crust–mantle boundary (P_mP). In a few record sections from instruments located at the northern flank of the Carnegie ridge deeper phases corresponding to the refraction within the uppermost mantle (P_n) can also be observed (e.g. Fig. 2a and f). Interestingly, P_mP is not observed in these record sections, thus we included the P_n phases to have an estimate of the crustal thickness in the northern flank of the ridge. The seismic phases can be easily followed up to more than 150 km from the source in most record sections (e.g. Fig. 2f). The reciprocity of traveltimes was checked out to verify the consistency of picked phases between different instruments.

The amplitude of the arrivals and the apparent velocities of the different phases identified in the record sections are very similar to those obtained in the data acquired across the Cocos and Malpelo ridge profiles during the PAGANINI-1999 experiment, which used the same sources and receivers (Sallarès *et al.* 2003). The refracted phase within the igneous crust (P_g) is observed as a strong arrival in all record sections and its pattern is similar in most of the instruments. At near offsets, it shows low apparent velocities (4–6 km s^{-1}), increasing quickly with distance to around 6.5 km s^{-1} at 20–30 km from the source, depending on the location of the instrument (Fig. 2). This segment of the phase is probably a refraction within the sediments and the basaltic upper igneous crust (oceanic layers 1 and 2), in which the vertical velocity gradient is likely to be strong as a result of the variations in rock porosity and alteration with depth (e.g. Detrick *et al.* 1994). Beyond this distance the apparent velocity of the P_g phase is more uniform, exceeding rarely 7.0 km s^{-1}. This flat segment of the phase is interpreted to be a refraction in the upper part of the lower igneous crust (oceanic layer 3), which is mostly composed of gabbros and is less porous and altered than layer 2.

The other phase observed in most record sections is the Moho reflection (P_mP). It is observed as a high-amplitude arrival, especially at the thickest crustal segments beneath the crest of the ridge. The main difference between the two profiles is the distance at which P_mP

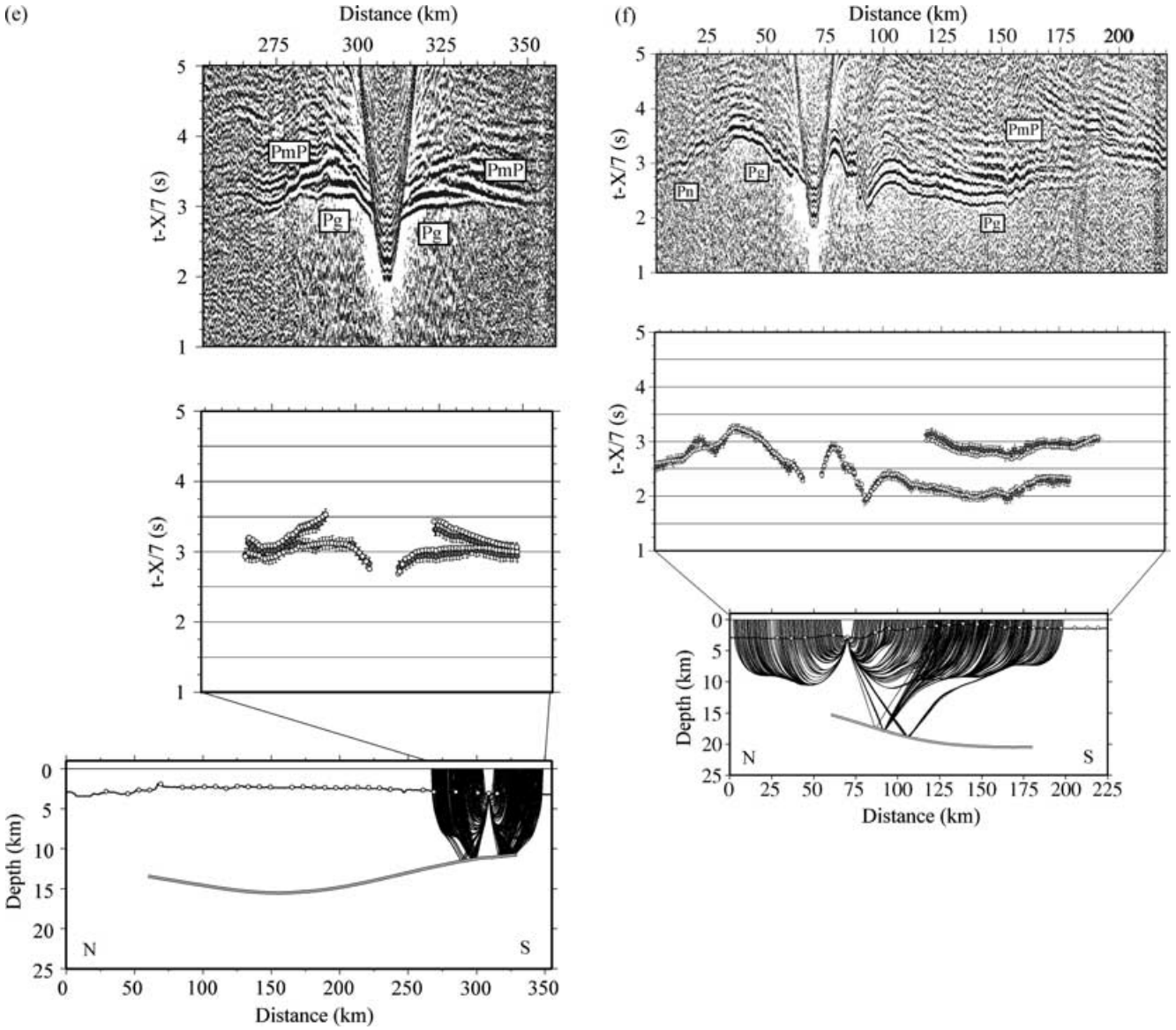

Figure 2. (*Continued.*)

becomes indistinguishable from P_g, which provides a qualitative estimation of the differences in crustal thickness along the two profiles. In profile 1, the distance is less than 80 km (Figs 2b and c), while in profile 2 it is as long as 150 km (Figs 2f and i), indicating that the crust is considerably thicker along profile 2. In the deep ocean basin located south of the Carnegie ridge, P_mP is observed at near-offsets (∼20 km), and P_mP and P_g become indistinguishable at approximately 30–40 km from the source (Fig. 2e). This is consistent with a reflection from the Moho of a fairly normal oceanic crust (7–8 km).

Picking of P_g and P_mP phases was done manually. Picking errors were assigned to be half a period of one arrival, to account for a possible systematic shift in the identification of the arrivals. In addition, they were overweighted or downweighted depending on the quality of the phase. For P_g phases, errors are around 40–50 ms for near offsets and 50–60 ms for far offsets. For P_mP phases, they are ∼80 ms on average.

4 SEISMIC TOMOGRAPHY

2-D velocity models along both profiles were estimated using the joint refraction and reflection traveltime inversion method of Korenaga *et al.* (2000). This method allows the determination of a 2-D velocity field together with the geometry of a floating reflector from the simultaneous inversion of first arrivals and secondary reflections traveltimes. The uncertainty of the obtained model parameters is estimated by performing a Monte Carlo–type analysis, which is identical to that described in Sallarès *et al.* (2003). The main steps of the inversion procedure are as follows: (i) A one-dimensional (1-D) averaged velocity model and a Moho depth are calculated. This model is used as a reference model to

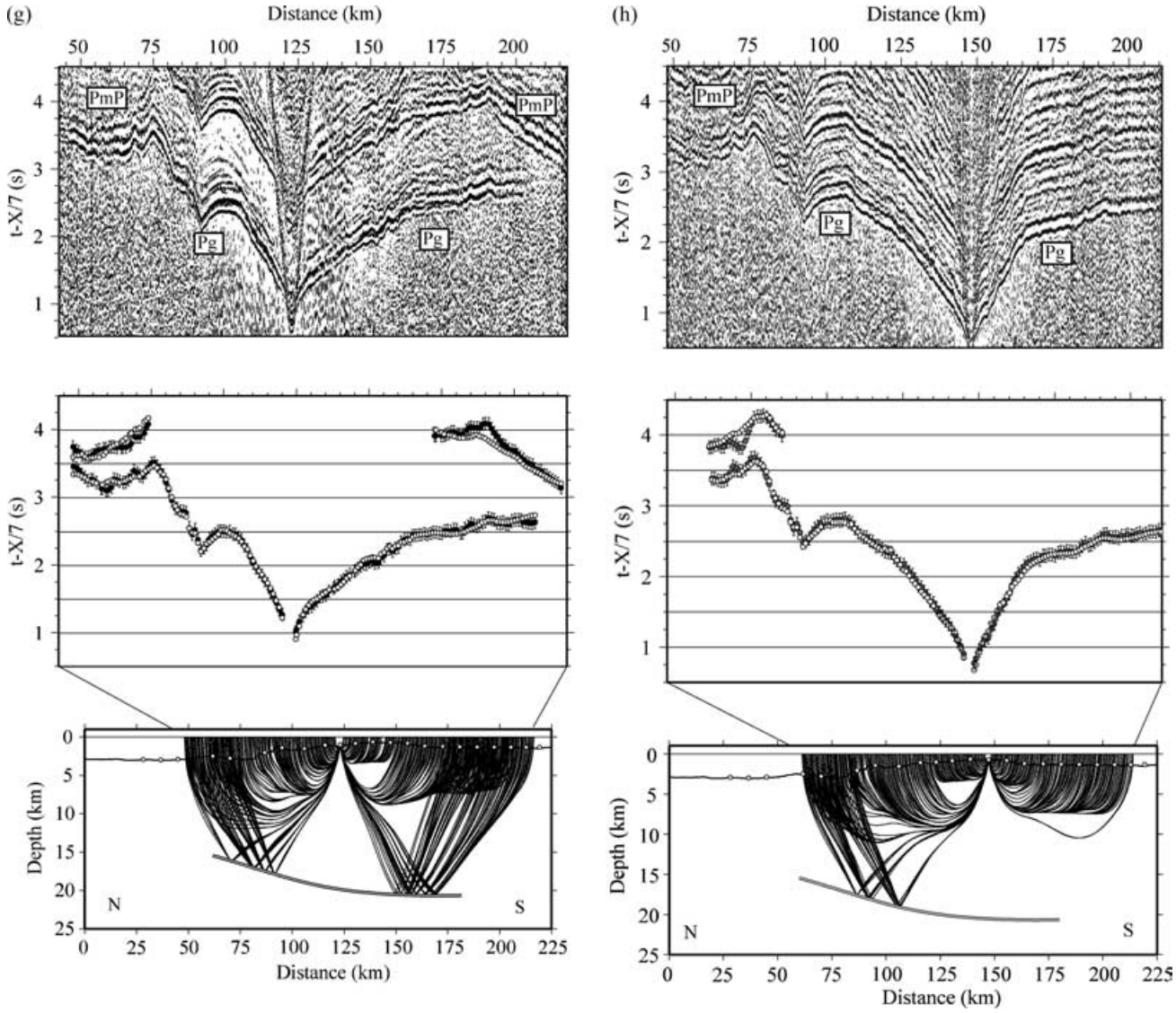

Figure 2. (*Continued.*)

perform the inversion. (ii) A set of 100 1-D initial models is constructed by randomly perturbing the Moho depth (±3 km) and the velocity of the crustal nodes (±0.3 km s^{-1}) of the 1-D reference model. Besides, 100 noisy data sets are built by adding random picking errors (±25 ms) to each arrival from the initial data set, together with common phase errors accounting for a possible systematic shift in the picking of a given seismic phase (±50 ms) and common receiver errors (±50 ms). (iii) The 2-D model is parametrized and a 2-D inversion is performed for each random initial model with a random data set.

Our preferred final solution along both profiles is the average of all the Monte Carlo realizations (Fig. 3). The standard deviation of velocity and depth parameters with respect to the final solution can be considered as a statistical measure of the uncertainties (Tarantola 1987; Matarese 1993). The trade-off between velocity and depth parameters has been tested by performing the inversion with different values of the depth-kernel weighting parameter, w (Korenaga *et al.* 2000). The internal consistency of the data set and the robustness of the obtained solution have been checked out by comparing the results of two inversions using only one half of the data in each. We also performed checkerboard tests with synthetic data to estimate the resolving power of the data set. For a more detailed description of the inversion procedure and parameters, see Sallarès *et al.* (2003).

4.1 Results

4.1.1 Inversion parameters

The data set of profile 1 is composed of 6667 P_g and 3682 P_mP picked from 30 record sections. The model is 360 km wide and 25 km deep. Horizontal grid spacing is 0.75 km and vertical grid spacing varies from 0.2 km at the seafloor to 1.5 km at the bottom of the model. Spacing of depth parameters is 1.5 km. We use horizontal correlation lengths varying from 8 km at the top of the model to 16 km at the bottom and

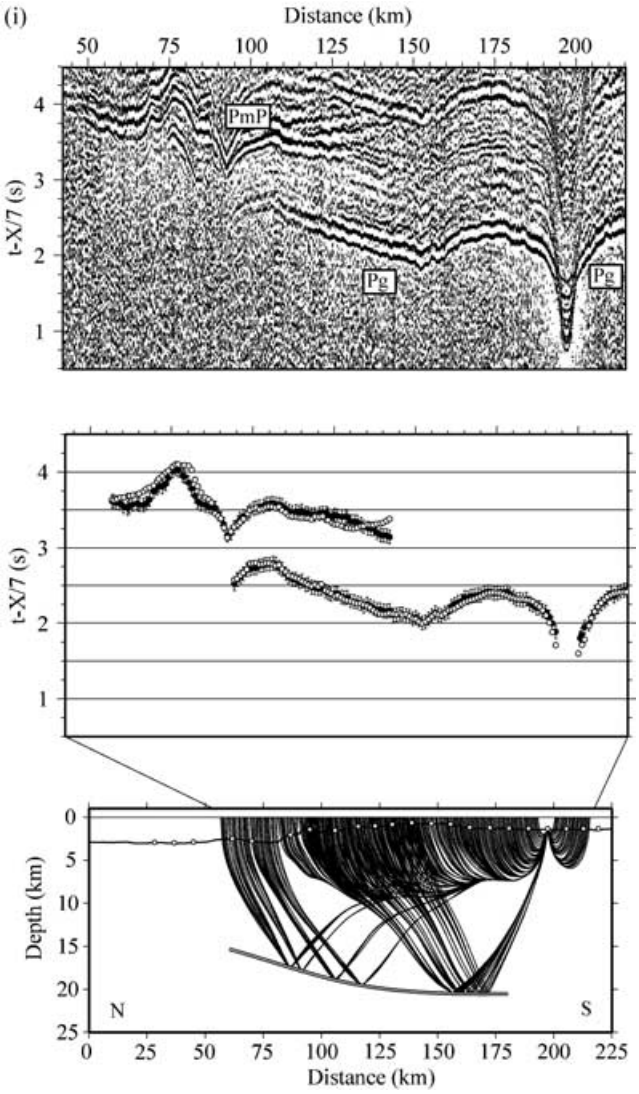

Figure 2. (*Continued.*)

vertical correlation lengths ranging from 0.2 km at the top to 3 km at the bottom for the velocity inversion. Variations of up to 50 per cent of these parameters lead to very similar results in terms of smoothness of the inverted velocity models. We tried three different values of $w = 0.1$, $w = 1$ and $w = 10$ for the depth weighting parameter. The rms traveltime misfit for the 1-D average model is 272 ms ($\chi^2 \sim 15$) and for the average model of all the 100 Monte Carlo realizations (with $w = 1$) it is 69 ms ($\chi^2 \sim 1.1$). In profile 2, the data set is composed of 5889 first arrivals and 2147 P_mP from 22 OBS and OBH. The model is 230 km wide and 25 km deep, grid spacing is 0.5 km horizontally, and it varies between 0.2 and 1.5 km vertically. Depth parameters are 1.5 km spaced. Horizontal and vertical correlation lengths are the same as those described for profile 1. Rms for the 1-D average model is 390 ms ($\chi^2 \sim 15$) and for the final model ($w = 1$) is 71 ms ($\chi^2 \sim 1.2$). The average velocity models of all the Monte Carlo realizations corresponding to both profiles are shown in Fig. 3. The fit between observed and calculated traveltimes and the ray tracing across the models for several instruments are shown together with the record sections in Fig. 2.

4.1.2 Seismic structure

The velocity structure is very similar along both profiles, and also analogous to that previously obtained at Cocos and Malpelo (Sallarès *et al.* 2003). The crust is divided into two layers, which can be identified with oceanic layers 2 (and the sediment cap) and 3. Layer 2 shows a notable vertical velocity gradient, with velocities varying from approximately 3.0 to 6.5 km s^{-1}. The isovelocity contour of 6.5 km s^{-1} corresponds to a major change in velocity–depth gradient that we attribute to the boundary between layers 2 and 3 (Fig. 3). In layer 3, velocity is much more uniform, and ranges between ~6.8 and ~7.2 km s^{-1}. Similarly to Cocos and Malpelo, the lowest layer 3 velocities are generally found where the crust is the thickest (i.e. beneath the crest of the ridge), although mean layer 3 velocities are not necessarily the same for a given crustal thickness in the different profiles. The maximum crustal thickness estimated along profile 1, located over 11–12 Myr old seafloor, is around 13 km, while along profile 2 (~20 Myr old seafloor) it is ~19 km (Fig. 3). Maximum crustal thickness estimated along their conjugated profiles

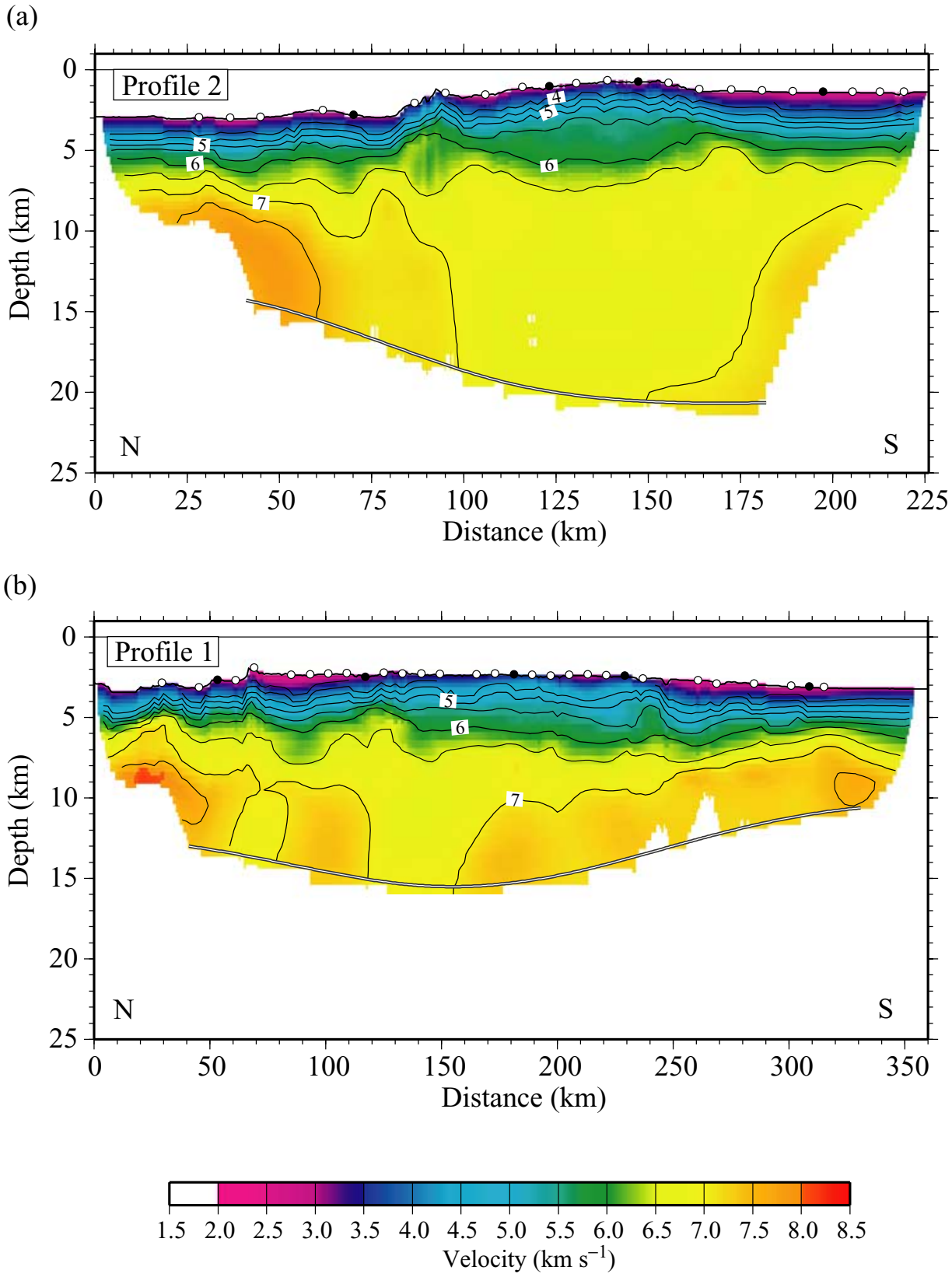

Figure 3. Seismic tomography results. Final averaged velocity models from the 100 Monte Carlo ensembles. (a) Profile 2, eastern Carnegie; (b) profile 1, western Carnegie. Open circles indicate ocean bottom seismometers (OBS)/ocean bottom hydrophones (OBH) locations. Solid circles show the instruments corresponding to the seismic gathers displayed in Fig. 2.

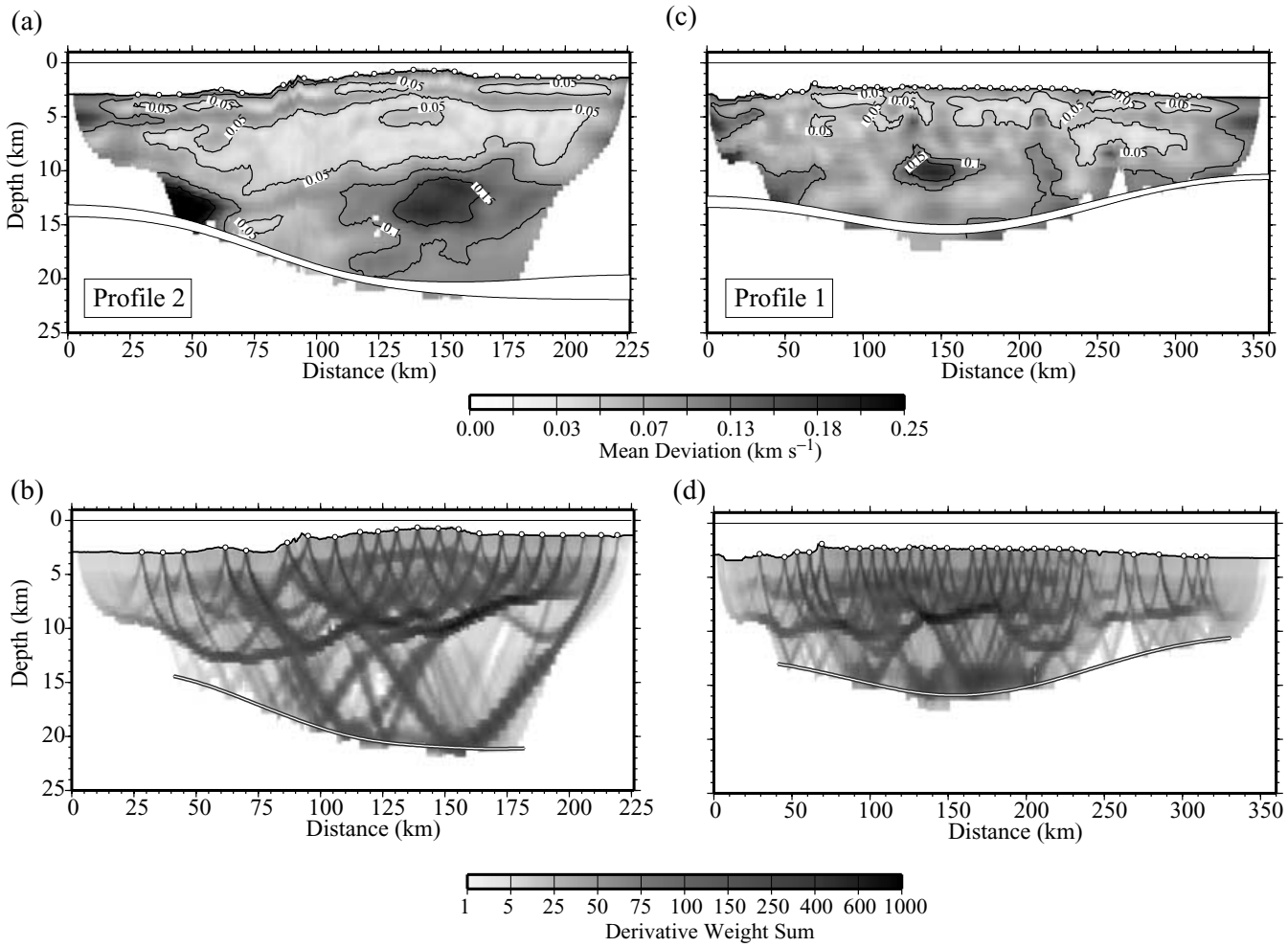

Figure 4. Velocity and Moho depth uncertainties corresponding to the average of the 100 Monte Carlo realizations (top) and derivative weight sum (DWS; bottom) obtained with the velocity models displayed in Fig. 3. (a, b) Profile 2, eastern Carnegie; (c, d) profile 1, western Carnegie.

acquired during the PAGANINI-1999 experiment (Fig. 1) are ∼16.5 km (12 Ma) and ∼19 km (20 Ma), respectively (Sallarès *et al.* 2003). The velocity structure obtained across the Carnegie ridge profiles is very similar to that obtained in another profile located south of the bulge of the Carnegie ridge, perpendicular to the trench axis, which extends from the outer rise to the coastline (Graindorge *et al.* 2003). This velocity model shows a crustal thickness of ∼14 km, with almost all the crustal overthickening accommodated in a 7.0–7.2 km s^{-1} crustal root that corresponds to the oceanic layer 3.

The similarity of the velocity structure across the different transects indicates that the process of formation of all the ridges (i.e. the nature of the GHS) is likely to be the same. Moreover, the crustal thickness variations reveal that the relative intensity of the GHS at both sides of the CNSC has changed with time, indicating the existence of significant variations in the relative distance between these two structures (Sallarès & Charvis 2003). The thickness of layer 2 is quite uniform (3.5 ± 1.0 km) regardless of the total crustal thickness variations. This means that the crustal thickening of the aseismic ridges is mainly accommodated by layer 3, in agreement with what is observed in most overthickened oceanic crustal sections (e.g. Mutter & Mutter 1993). The only exception to this general tendency is the northern flank of the Carnegie ridge, where layer 2 (and the whole crust) is significantly thinner than in the other parts of the transects. Here, the Moho geometry is not controlled by P_mP, but the presence of a conspicuous shallow (<8 km depth) and high-velocity (∼7.5–8.0 km s^{-1}) mantle-like anomaly indicates that the oceanic crust must be only 6–7 km thick (Fig. 3). Therefore, the Moho geometry could be highly asymmetric, showing a steeper transition between the crest of the ridge and the adjacent oceanic basin in the northern flank of the ridge (i.e. that which is closest to the CNSC) than in the southern flank. A similar type of behaviour was also observed in the conjugated segment of profile 1 over the Cocos ridge, where a steeper transition is observed in the inner, SE flank of the ridge, than in the outer, NW flank (Sallarès *et al.* 2003).

4.1.3 Uncertainty analysis

The statistical uncertainties of model parameters obtained by averaging the solutions of all 100 Monte Carlo realizations for both profiles are shown in Figs 4(a) and (c). The derivative weight sum (DWS), which is the column-sum vector of the Fréchet partial derivatives matrix (Toomey & Foulger 1989), is shown in Figs 4(b) and (d). Velocity uncertainty is lower than 0.1 km s^{-1} within most parts of the models.

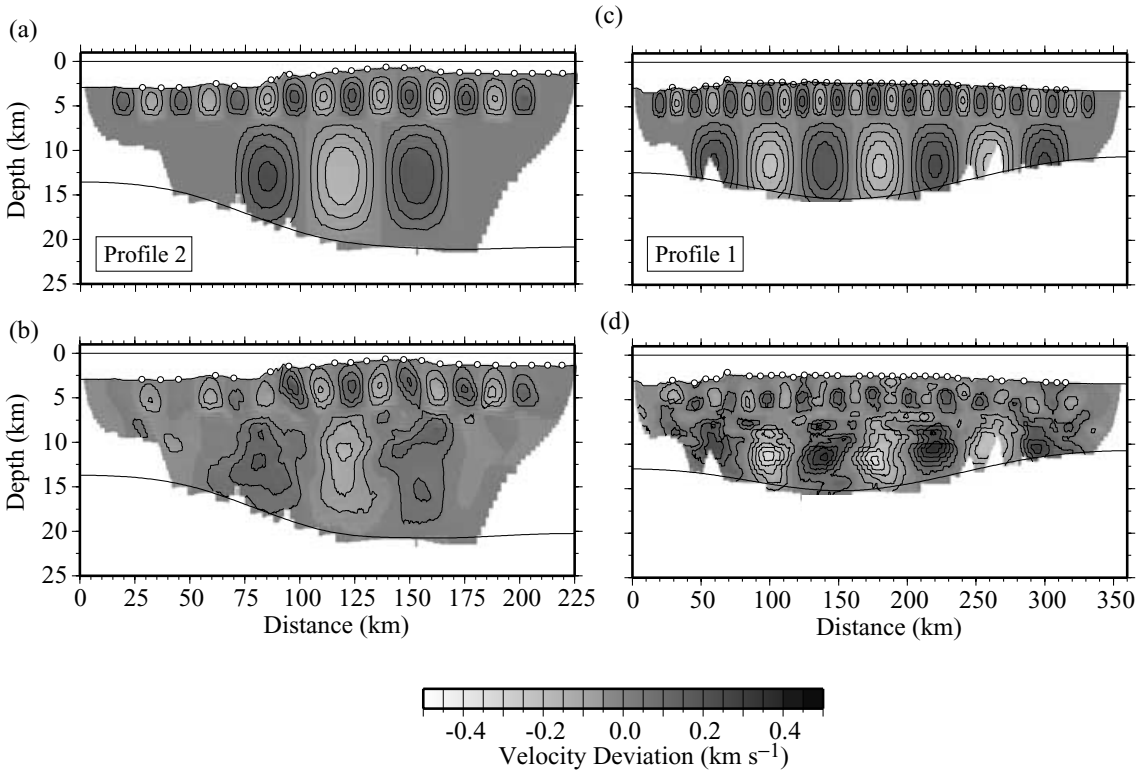

Figure 5. Results of the checkerboard tests. Synthetic models showing the amplitude of velocity anomalies with respect to the background models displayed in Fig. 3 (top) and results of tomographic inversion (bottom). (a, b) Profile 2, eastern Carnegie; (c, d) profile 1, western Carnegie.

Layer 2 velocities show generally the lowest uncertainties (<0.05 km s^{-1}). However, uncertainties are slightly higher in the upper half of this layer, where velocity gradient is larger, than in the bottom half. Uncertainties in layer 3 are generally smaller than 0.1 km s^{-1}, with several local anomalies where uncertainty is somewhat larger (∼0.15–0.20 km s^{-1}). Depth uncertainties are lower than 0.3–0.4 km along most of the section. The largest velocity (>0.2 km s^{-1}) uncertainties are obtained in the layer 3 of the northern segment of profile 2 (near 50 km model distance). Consistently, P_mP phases are not observed in this part of the transect. In layer 2, velocity can be well determined from P_g traveltimes. In contrast, P_g phases rarely go through the lower part of layer 3 (Figs 4b and d), so both the lower crustal velocity and Moho geometry information are contained uniquely in P_mP traveltimes. Because inversions with reflection traveltimes are subject to velocity–depth ambiguities, the Moho depth and lowermost crust velocity uncertainties tend to be correlated, as can be observed in Fig. 2(a).

4.1.4 Resolution and accuracy

A classical manner to estimate the resolving power of a given data set with a particular experiment layout is to perform checkerboard tests. We have built a reference model by adding sinusoidal anomalies with a maximum relative amplitude of 5 per cent to our preferred solution in the upper crust (13 × 6 km) and lower crust (35 × 12 km). The reference model and the inverted solution for both profiles are shown in Fig. 5. The inversion with synthetic data was performed using as an initial model a 1-D crustal velocity model with a flat Moho, corresponding to the best fit of all traveltimes. The data set constitutes the traveltimes calculated with the reference model, to which we added picking, common phase and common shot errors (see description in Section 4). The pattern of the velocity anomalies is well recovered at both upper and lower crustal levels. In general, we can conclude that teometry of the experiment is appropriate and thus the data set is sensitive enough to resolve velocity anomalies of the size considered here, with lateral velocity contrasts lower than 0.2 km s^{-1} in the upper crust and lower than 0.3 km s^{-1} in the lower crust. Moreover, the Moho geometry is well recovered along most of the model with differences lower than 0.4 km, in agreement with the results of the uncertainty analysis. However, checkerboard tests are an incomplete demonstration of the degree of the ambiguities, because they are always limited to very specific velocity models with particular anomalies. Instead, Korenaga *et al.* (2000) proposed a practical way to do that by systematically exploring the result of the inversion using different values for the depth-kernel weighting parameter, w, which controls the relative weighting of velocity and depth parameters in reflection tomography. We did the test using $w = 0.1$ and $w = 10$. The results are very similar to those obtained with $w = 1$, showing always the overall anticorrelation between crustal thickness and layer 3 velocity, which indicates that velocity–depth trade-off is not important and it does not alter the main results of the work. Finally, we performed a last test to evaluate the consistency of the results in profile 1, which consisted of repeating the inversion twice with the 1-D average model as an initial model but using only the data from one half of the instruments on each inversion. The results are shown in Fig. 6. The long-wavelength structure obtained using both data sets is very similar, showing the same crustal thickness and similar features along

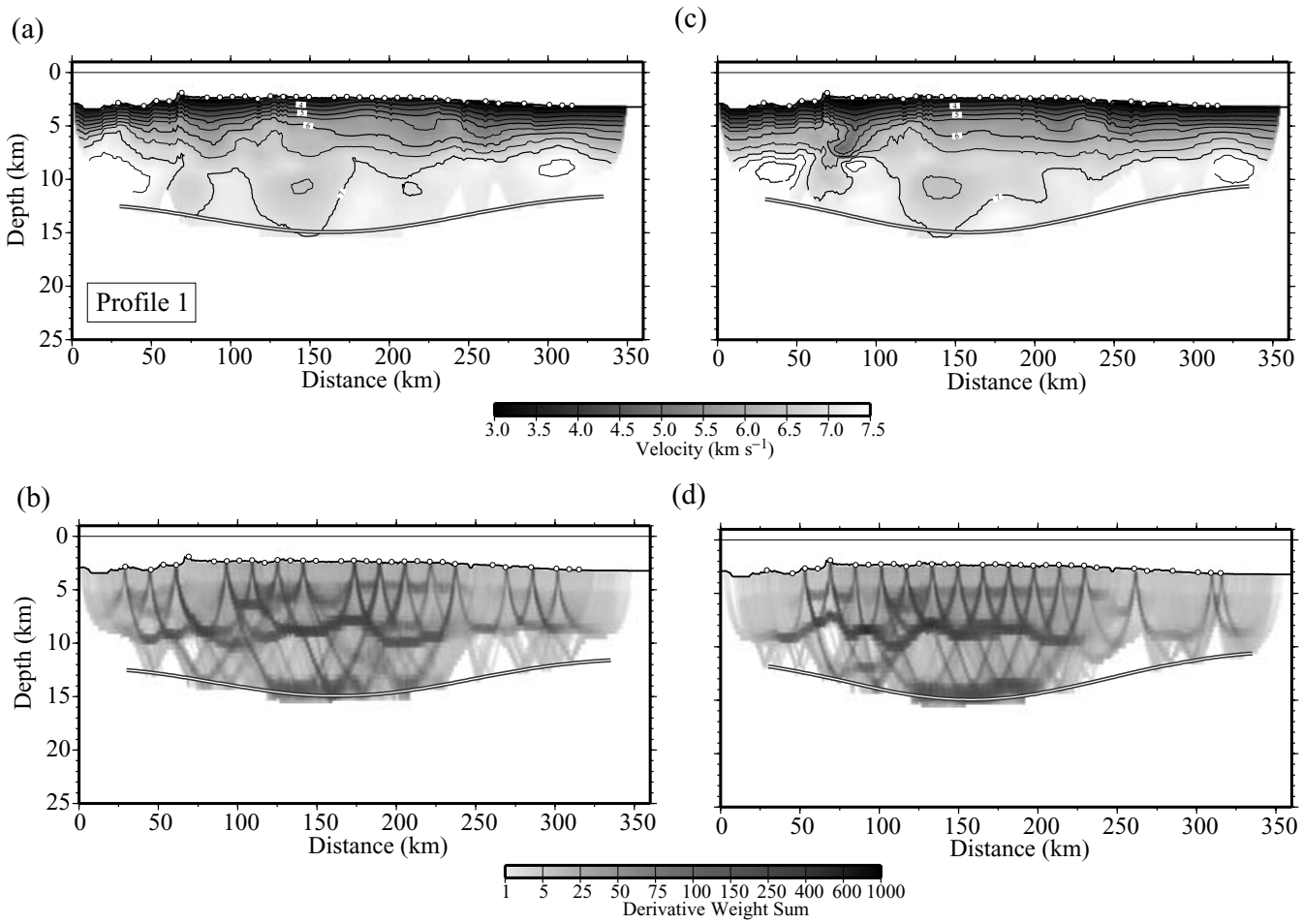

Figure 6. Results of two inversions using only one half of the instruments on each. Velocity models (top) and derivative weight sum (DWS; bottom) obtained using 15 Geomar ocean bottom hydrophones (OBH; a, b), and with 13 Institut de Recherche pour le Développement (IRD) ocean bottom seismometers (OBS) and 2 Geomar OBH (c, d).

the whole profile. Differences are local and small. The remarkable resemblance of the solutions obtained using two totally independent data subsets confirms the internal consistency of the whole data set, and demonstrates that most velocity anomalies are real features and that inversion artefacts, if present, are minor.

5 GRAVITY AND COMPENSATION OF TOPOGRAPHY

Large igneous provinces and aseismic ridges typically show broad swells, which are characterized by striking topography and gravity anomalies (Schilling 1985; Sleep 1990). Swells are believed to be supported by a combination of crustal thickening and sublithospheric mantle density anomalies of thermal and/or chemical origin (Oxburgh & Parmentier 1977; Courtney & White 1986; Phipps Morgan *et al.* 1995), but the relative importance of each factor to support the swell is a matter of discussion. One end-member is the mantle plume model, which affirms that the primary sources of plume buoyancy are mantle thermal anomalies (White & McKenzie 1989, 1995). Another alternative is a combination of hotter than normal mantle temperatures and mantle density variations arising from melt depletion (Phipps Morgan *et al.* 1995). In both cases, the mantle column beneath hotspot swells would have to show anomalous seismic velocities and densities related with the presence of the mantle plume. The contribution of the mantle anomalies is likely to be significant for oceanic swells located above active hotspots or melting anomalies, as indicated by seismic and gravity data in Iceland (Wolfe *et al.* 1996; Darbyshire *et al.* 2000), Hawaii (Laske *et al.* 1999) and the present-day GHS-influenced area (Canales *et al.* 2002; Hooft *et al.* 2003).

The other end-member is the crustal compensation model, in which the swell is largely compensated by lateral variations of crustal density and Moho topography, with a minor contribution of mantle density anomalies. This seems to be the case, for instance, of the Marquesas swell, where buoyancy of the material underplating the island chain has been shown to be able to support almost completely the swell (McNutt & Bonneville 2000). These authors suggested that this can be also the case for other swells, such as Hawaii or the Canary Islands. In this case, the upper-mantle velocity and density anomalies are likely to be small, perhaps undetectable for seismic methods. The crustal compensation may be a plausible model to account for oceanic swells located away from the zone of direct influence of the mantle plume. This is apparently the case of the Cocos and Malpelo ridges, in the GVP (Sallarès *et al.* 2003), although a previous gravity analysis of the GVP suggests that mantle

density anomalies associated with the presence of the GHS are still significant ∼8 Myr after the emplacement of the ridge and ∼400 km away from the hotspot location (Ito & Lin 1995). Between the two end-member cases, there are a number of different possibilities. Canales *et al.* (2002), for example, argued that the Galápagos swell is sustained by a combination of crustal thickening (∼50 per cent), thermal buoyancy (∼30 per cent) and chemical buoyancy arising from melt depletion (∼20 per cent).

In this section, we show the results of a gravity analysis along profile 1 (Fig. 1). We chose this profile because it is located mid-plate, far away from the margin, and the assumption of lateral homogeneity is valid in this case. Our purpose is to calculate the velocity-derived crustal density structure, and to estimate then the range of mantle density anomalies required to explain the observed gravity and topography data along the profile. Velocity-derived density models across Malpelo and Cocos are also available in Sallarès *et al.* (2003). The similarity of the crutal structure between this profile and the other profiles acquired in Carnegie, Cocos and Malpelo, makes it possible to extrapolate the results obtained to the other ridges of the GVP.

5.1 Density models and gravity analysis

The gravity profile along the transect has been built using available marine gravity data based on satellite altimetry (Sandwell & Smith 1997). We have employed a code based on the Parker (1972) spectral method to calculate the gravity anomaly produced by a heterogeneous 2-D density model. We first calculated the gravity anomaly generated by a single crustal layer with the crust–mantle boundary geometry from the velocity model and uniform density (2800 kg m^{-3}). This model fits the observed anomaly with a misfit of ∼30 mGal, but it underestimates the anomaly at the centre of the ridge and at the northern flank, where the Moho geometry derived from seismic tomography is worst resolved. In the second model, the velocity model from Fig. 3(a) was directly transformed to densities using different empirical conversion laws for the different crustal layers. For velocities lower than 3.2 km s^{-1} (which we considered to be sediments), we have applied the velocity–density relationship of Hamilton (1978) for shale, $\rho = 0.917 + 0.747Vp - 0.08Vp^2$, while for higher velocities we have assumed Carlson & Herrick's (1990) empirical relation for oceanic crust, $\rho = 3.61 - 6.0/Vp$, which is based on Deep Sea Drilling Project (DSDP) and Ocean Drilling Program (ODP) core data. Mantle density has been fixed to 3300 kg m^{-3}. Following the procedure described in Sallarès *et al.* (2003), we have calculated the densities from seismic velocities at *in situ* conditions using the estimates of the pressure and temperature partial derivatives (e.g. Korenaga *et al.* 2001). Because the Moho geometry of the northern flank of the ridge (0–75 km along profile) is poorly constrained by the seismic data, we have varied the Moho depth in this part of the transect until a good match of the gravity data has been obtained.

The estimated density model (Fig. 7a), shows a highly asymmetric Moho geometry. The transition between the top of the bulge and the adjacent oceanic basin is more abrupt in the northern flank of the ridge than in the southern flank. In the north, the oceanic basin is ∼6 km

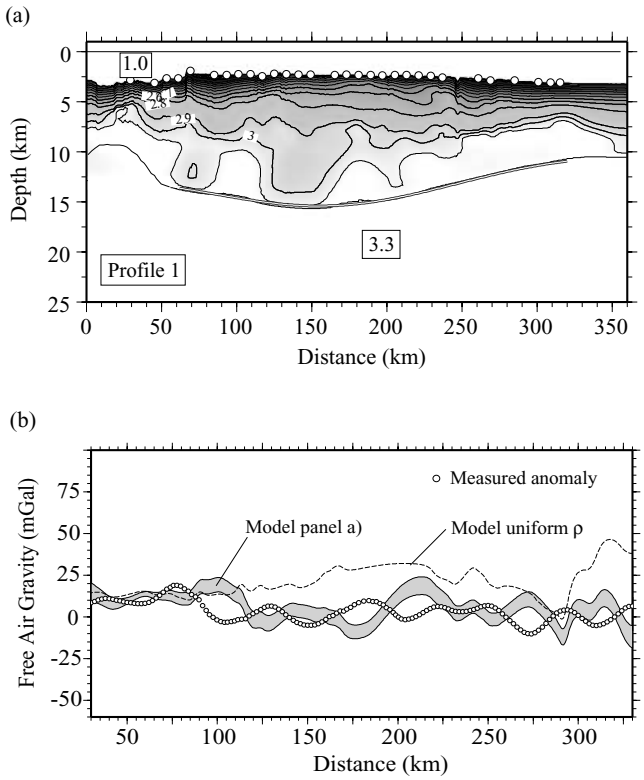

Figure 7. (a) Velocity-derived density model along profile 1, western Carnegie. Densities are in g cm^{-3}. (b) Observed free-air gravity anomaly (open circles) and calculated gravity anomaly for model displayed in panel (a). Shaded zone shows the gravity anomaly uncertainty inferred from the Monte Carlo analysis. The rms misfit for this model is 6 mGal. Dashed line corresponds to the constant density model (2800 kg m^{-3}) with the Moho obtained from the tomographic inversion.

thick, while in the south the crust is ∼8 km thick. The velocity-derived density model explains the observed gravity anomaly with a misfit of less than 6 mGal, indicating that the velocity model is compatible with the gravity data within the model uncertainty without the necessity of considering mantle density anomalies (Fig. 7b). The results are thus consistent with those previously obtained in the Cocos and Malpelo ridge profiles (Sallarès *et al.* 2003).

5.2 Isostasy model

Along with the gravity analysis described in the previous section, we have performed an analysis of the bathymetric data in order to determine if the velocity-derived density models of the Carnegie, Cocos and Malpelo ridges are also compatible with the depth anomalies observed along the transects. We assumed in our analysis that the system of interest is isostatically compensated. Topography compensation studies assume isostatic equilibrium either as a product of crustal thickness variations (i.e. Airy isostasy), as a product of lateral variations in the mantle density above a given compensation depth (i.e. Pratt isostasy), or, more likely, as a combination of both effects (e.g. Ito & Lin 1995; Escartín *et al.* 2001; Canales *et al.* 2002). In the previous section, we have shown that lateral crustal density variations can contribute significantly to the observed gravity anomaly, so we have also included the effect of the lateral density variations in our calculations. The long-wavelength

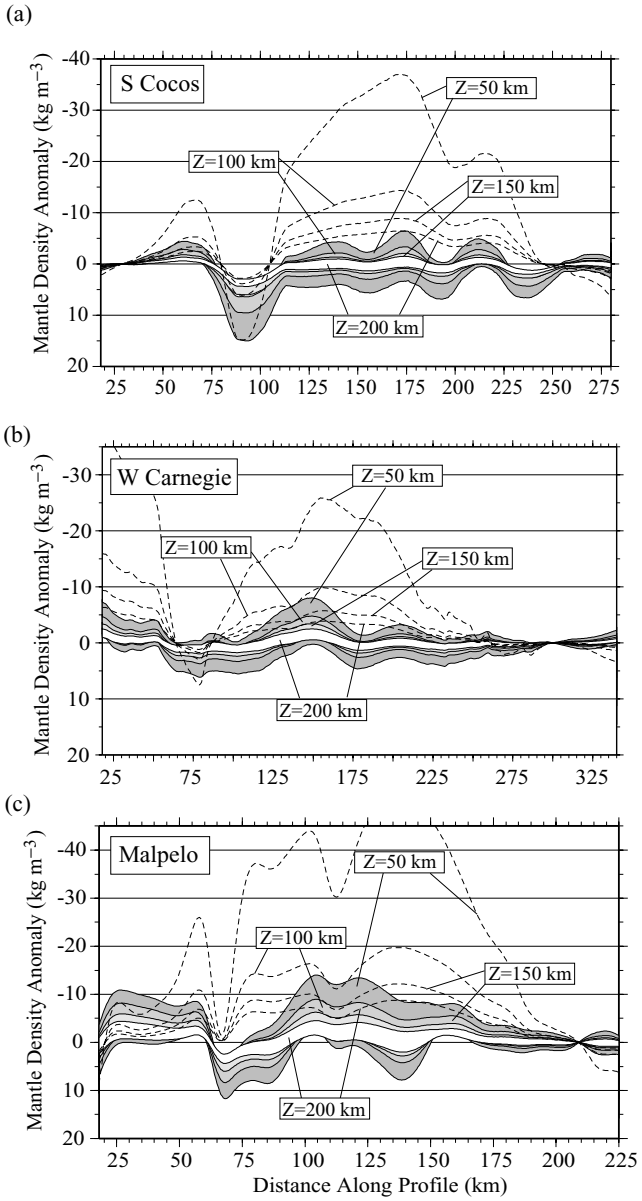

Figure 8. Mantle density variations along Cocos (a), Carnegie (b) and Malpelo (c) transects, inferred from the isostasy model, for different values of the compensation depth, $Z = 50$, 100, 150 and 200 km. Cocos and Malpelo profiles correspond to the crustal density models shown in Sallarès *et al.* (2003). Carnegie profile corresponds to the crustal density model from Fig. 7(a). Shaded stripes show the mantle density uncertainty inferred from the Monte Carlo analysis for each compensation depth. Dashed lines correspond to uniform crustal density models (2800 kg m^{-3}) with the Moho geometry obtained from seismic tomography along the same transects.

structure along the profiles has been calculated by averaging the seafloor depth, crustal thickness and crustal density within a 25-km-wide laterally moving window. In that case, differences in mantle density between a lithospheric column at a given position, x, and a reference column at x_0, $\Delta\rho_m(x)$, can be therefore expressed from a mass balance as follows:

$$\Delta\rho_m(x) = \frac{\Delta\rho_{mw}\Delta h_w(x) + \Delta\rho_{mc}(x)\Delta h_c(x)}{Z - h_w(x) - h_c(x)}, \quad (1)$$

where

$$\Delta\rho_m(x) = \overline{\rho_m}(x) - \overline{\rho_m}(x_0),$$

$$\Delta\rho_{mw} = \overline{\rho_m}(x_0) - \rho_w,$$

$$\Delta h_w(x) = h_w(x) - h_w(x_0),$$

$$\Delta\rho_{mc}(x) = \overline{\rho_m}(x_0) - \overline{\rho_c}(x),$$

$$\Delta h_c(x) = h_c(x) - \frac{\Delta\rho_{mc}(x_0)}{\Delta\rho_{mc}(x)} h_c(x_0),$$

and ρ_w is water density, $\overline{\rho_c}(x)$ and $\overline{\rho_m}(x)$ are the averaged crustal and mantle densities, $h_w(x)$ is the water depth and $h_c(x)$ is the crustal thickness, of a lithospheric column located at x. The definition and value of all constants and variables used in the model is given in Table 2.

The only unknown in eq. (1) is thus Z, the compensation depth above which we assume that all lateral density anomalies are confined. We have estimated the mantle density variations required, $\Delta\rho_m(x)$, to fit the observed bathymetry along the density models estimated at profile 1 in Carnegie (Fig. 7a), and at profiles 1 and 3 in Cocos and Malpelo (figs 10d and 12a in Sallarès *et al.* 2003). Uncertainty of the calculated mantle density anomalies is the mean deviation of the results obtained using all the velocity models from the Monte Carlo realizations. In order to estimate the effect of lateral crustal density anomalies, we have compared the results with those obtained for the constant density models (2800 kg m^{-3}) using the seismic-derived crustal geometry estimated along these profiles. The results obtained for different compensation depths, $Z = 50$,100, 150 and 200 km, along the three profiles are shown in Fig. 8.

Results show that the contribution of lateral crustal density variations is also significant to account for the depth anomaly. Hence, the predicted mantle density anomalies for the variable crustal density models along the three transects are negligible considering the range of uncertainty of the velocity models (between $\sim 0 \pm 5$ kg m^{-3} for $Z = 50$ km and $\sim 0 \pm 1$ kg m^{-3} for $Z = 200$ km). This means that the swell anomaly is isostatically compensated at the base of the crust and that mantle density anomalies, if present, have to be small, $<$5–10 kg m^{-3}, which is under the uncertainty threshold of the method. In contrast, models considering a constant density crustal layer (even with the correct Moho geometry) predict much larger mantle density anomalies beneath the thickened part of the crust, as high as 40–50 kg m^{-3} for $Z =$ 50 km in the thickest part of the Cocos and Malpelo ridges (Figs 8a and c).

In conclusion, the results show that the upper-mantle density structure beneath the GVP aseismic ridges is uniform and shows typical mantle density ($\sim$3300 kg m^{-3}) for a wide range of compensation depths (50–200 km), suggesting that these ridges are isostatically compensated at the base of the crust. This means that mantle density anomalies, if they once existed, are insignificant for ages greater than 10 Myr. This result is very different from that obtained by Ito & Lin (1995) based on the analysis of the gravity signatures along the present- and palaeo-axes ($<$8 Myr) of the CNSC. Ito & Lin (1995) corrected the gravity field for topography and for an estimated crust–mantle boundary, and they associated the remaining gravity anomaly to the presence of mantle density anomalies of thermal origin. The main difference with our work is that they assumed the lateral crustal density variations along their profiles to be negligible. However, as we have shown above, this is not the case. The inclusion of lateral crustal density variations accounts for the gravity and topography anomalies across the GVP aseismic ridges without calling for anomalous mantle densities (and temperatures). This seems to indicate that the significance of compositional mantle buoyancy as a result of melt extraction and depletion (e.g. Oxburgh & Parmentier 1977) is smaller than suggested by previous studies performed in the region (e.g. Canales *et al.* 2002). However, it is not straightforward to compare the work of Canales *et al.* (2002) with ours, because they focussed their study on the present-day axis of the CNSC, while we refer to structures formed more than 10 Ma. In any case, our results show that any estimation of the mantle density structure from gravity and topography analysis for regions showing prominent variations in crustal thickness and topography, such as aseismic ridges, would have to include a correction for lateral crustal density contrasts.

6 NATURE OF THE GALÁPAGOS HOTSPOT

The amount of melt produced by adiabatic decompression of the mantle and the composition of the resultant igneous crust are known to depend on:

(i) the temperature (Klein & Langmuir 1987; White *et al.* 1992), composition (e.g. Korenaga & Kelemen 2000) and water content (Ito *et al.* 1999; Braun *et al.* 2000) of the mantle source; and

(ii) the mechanical constraints bounding the extent of the mantle melting zone (i.e. the presence of a lithospheric lid; e.g. Watson & McKenzie 1990; Korenaga *et al.* 2002; Fig. 9a).

Table 2. Definition, units and values of all the constants and variables used throughout the calculations.

Variable	Definition (units)	Value
$\Delta\rho_m(x)$	Mantle density variation between a column located at x and a reference column located at x_0 (kg m^{-3})	
$\overline{\rho_m}(x_0)$	Vertically-averaged reference mantle density at x_0 (kg m^{-3})	3300
$\overline{\rho_m}(x)$	Vertically-averaged mantle density at x (kg m^{-3})	
$\Delta\rho_{mc}(x)$	Crust–mantle density contrast at x (kg m^{-3})	
$\overline{\rho_c}(x)$	Vertically averaged crustal density at x (kg m^{-3})	
$\Delta h_c(x)$	Crustal thickness variation between x and x_0 corrected for density contrast (km)	
$h_c(x)$	Crustal thickness at x (km)	
$\Delta h_w(x)$	Seafloor depth variation between x and x_0 (km)	
$h_w(x)$	Seafloor depth at x (km)	
Z	compensation depth (km)	50–200
P_0	Initial pressure of melting (GPa)	
T_0	Temperature at P_0 (°C)	
T_p	Mantle potential temperature (°C)	
F	Melt fraction (per cent)	
Γ	Melt productivity (per cent GPa^{-1})	
Γ_d	Melt productivity in the primary melting zone (per cent GPa^{-1})	10–20
Γ_w	Melt productivity in the hydrous melting zone (per cent GPa^{-1})	0.5–2.0
z_0	Initial depth of anhydrous melting (km)	
z_f	Final depth of melting (km)	
θ	Angle of the lithospheric boundary	45°
g	The standard gravity acceleration of the Earth (m s^{-2})	9.8
H	Crustal thickness (km)	
b	Thickness of the lithospheric lid (km)	
V_p	Compressional wave velocity of the igneous crust (km s^{-1})	
ρ_m	Average mantle density (kg m^{-3})	3300
ρ_c	Average crustal density (kg m^{-3})	2900
$\dot{m}$	Melting rate (per cent Myr^{-1})	
$\dot{M}$	Total melt production (per cent Myr^{-1})	
R	Mantle melting region	
w	Mantle upwelling rate (km Myr^{-1})	
u_0	Seafloor spreading rate (km Myr^{-1})	60
χ	Mantle upwelling ratio	
X	Upwelling ratio at the base of the mantle melting region	
α	Factor of upwelling ratio decay	$1/X$ to 1
Δz	Thickness of the hydrous melting zone (km)	50–75
$\bar{F}$	Mean fraction of melting (per cent)	
$\bar{Z}$	Mean depth of melting (km)	

McKenzie & Bickle (1988) demonstrated that the oceanic crust of 6–7 km thick and MORB-like composition normally originated at a spreading centre is the result of decompression melting of a mantle source composed of dry pyrolite with a potential temperature of ∼1300°C. In this case, the crustal accretion is considered to be only a passive response to seafloor spreading (i.e. passive upwelling). Higher mantle temperatures or compositional anomalies may cause buoyant upwelling of the mantle (i.e. active upwelling; e.g. Ito *et al.* 1996). The combination of active upwelling and higher mantle temperatures, or the presence of a more fertile mantle source, will produce larger amounts of melting and, eventually, a thicker crust. Generally, melt anomalies are considered to have a thermal origin rather than a compositional one, in accordance with the original hotspot hypothesis (Wilson 1963; Morgan 1971). Because the MgO content of melt increases as mantle temperature rises above normal and seismic velocities of igneous rocks are proportional to their MgO content, igneous crust produced by a thermal anomaly should also display higher velocity than normal oceanic crust (White & McKenzie 1989). This hypothesis works well in a number of cases and has been repeatedly invoked to explain the origin of high-velocity crustal roots found in aseismic ridges (e.g. Grevemeyer *et al.* 2001; Walther 2002), oceanic plateaux (Coffin & Eldholm 1994; Charvis *et al.* 1995; Charvis & Operto 1999; Darbyshire *et al.* 2000) or passive volcanic margins (e.g. Kelemen & Holbrook 1995; Barton & White 1997). However, as we stated in Section 1, two recent wide-angle seismic studies performed in the North Atlantic volcanic province (Korenaga *et al.* 2000) and in the Galápagos province (Sallarès *et al.* 2003 and this study) have shown that lower igneous crust can also have normal or lower than normal seismic velocities, thus contrary to what conventional plume theory predicts. By comparing those results with the predictions of a mantle melting model based on empirical relationships between the seismic velocity of compressional waves, and the mean pressure and fraction of melting (Korenaga *et al.* 2002), Sallarès *et al.* (2003) suggested that other parameters such as active upwelling or major element compositional anomalies can be more significant than mantle temperatures to account for the excess of melting. Another option that is not contemplated in the model of Korenaga *et al.* (2002) is the possible influence of deep damp melting. It has been suggested that damp melting between the dry and wet solidus for a volatile-bearing mantle (∼70–120 km deep) may constitute a significant part of the total volume of melt, even if the melting rate is an order of magnitude

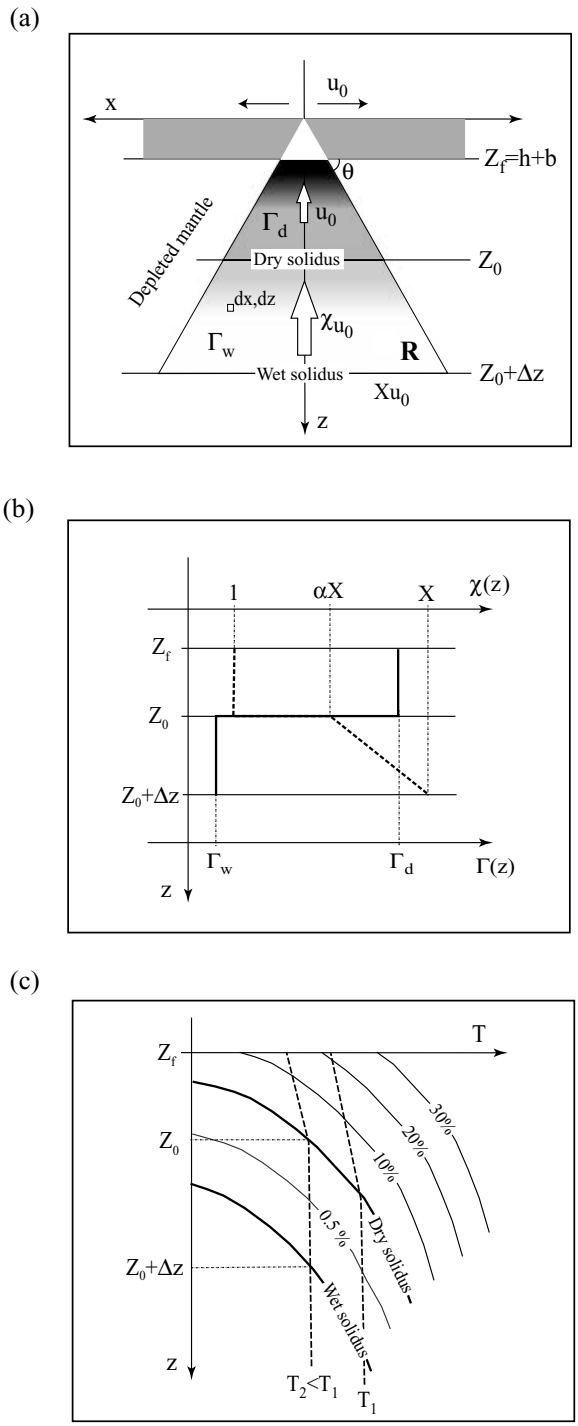

Figure 9. (a) Sketch summarizing the melting process for mantle corner flow beneath spreading ridges. U_0 is the spreading rate and χ is the mantle upwelling ratio. In our model, $\chi = 1$, passive upwelling, above the dry solidus. The final depth of melting is Z_f, which is determined by the lithospheric lid (old lithosphere, b, and newly formed oceanic crust, h). The initial depth of melting is Z_0, which is defined by the intersection of the dry solidus and the mantle adiabat. ΔZ is the thickness of the damp melting area. R is the section of the melting region for mantle corner flow, dx, dy indicate an element of mantle. (b) Diagram indicating the values of the upwelling ratio at the base of the melting zone, X, the slope of the upwelling ratio decay within the damp melting zone, α, and the melt productivity within the dry, Γ_d, and damp, Γ_w, melting regions in our melting model (see details in Sections 6.1 and 6.2). The thick solid line represents the melt productivity, Γ (z), and the thick dashed line the upwelling ratio, χ (z). (c) Scheme of a phase diagram illustrating the dry and wet solidus (thick solid lines), the mantle adiabats for different potential temperatures (dashed lines), and the melting rates for given Γ_d and Γ_w (thin solid lines).

lower than that of dry melting (Hirth & Kohlstedt 1996; Braun *et al.* 2000), if it is coupled with vigorous upwelling at the base of the melting zone (e.g. Maclennan *et al.* 2001). Accordingly, numerical models indicate that the viscosity increase associated with dehydration prevents buoyancy forces from contributing significantly to mantle upwelling above the dry solidus, and thus the upwelling in the primary melting zone is mostly passive and the melt production consequently lowers in this zone of the melting region (Ito *et al.* 1999). The results of a recent geophysical and geochemical study along the CNSC suggest that deep damp melting may be the most significant factor to account for the excess of magmatism associated to the presence of the GHS (Detrick *et al.* 2002; Cushman *et al.* 2005).

In the next section, we develop a mantle melting model including the effect of mantle temperature, deep damp melting, active upwelling beneath the dry solidus and mantle source composition, in order to quantify the relative significance of the different melting parameters on the seismic structure of the resultant igneous crust. The final purpose is to compare the results with those obtained in the different aseismic ridges of the GVP in order to determine the most plausible nature of the GHS.

6.1 Mantle melting model

Our mantle melting model is based on that previously developed by Korenaga *et al.* (2002), in which a connection between the parameters describing mantle melting processes and the resultant crustal structure is established on the basis of an empirical relationship between crustal velocity and the mean pressure and degree of melting. They considered a 1-D steady-state melting model including the effects of mantle potential temperature, active upwelling and considering the presence of a lithospheric lid. The main differences between their model and ours are as follows:

(i) we consider a 2-D steady-state model to describe the triangular melting regime resulting from mantle corner flow (e.g. Plank & Langmuir 1992);

(ii) we calculated the mean degree of melting as the average degree of melting of all the individual parcels of melt pooled in the crust (Forsyth 1993; Plank *et al.* 1995);

(iii) we included the effect of deep damp melting (Hirth & Kohlstedt 1996; Braun *et al.* 2000); and

(iv) we restricted active upwelling to beneath the dry solidus, according to the calculations of Ito *et al.* (1999).

Our model does not represent a rigorously based physical model; it is only an approximation to estimate the relative importance of the different parameters that characterize the mantle melting process. We have chosen this model representative of melting beneath an oceanic ridge because four of the five profiles that we have modelled correspond to aseismic ridge segments that were emplaced at the spreading axis as a result of hotspot–ridge interaction (Sallarès & Charvis 2003). The only exception is the southern Cocos profile (Fig. 8a), which is probably the result of an initial phase of on-ridge emplacement of a thicker than normal crust (∼13 km), and a second phase of off-ridge thickening (∼3.5 km) when the aseismic ridge passed over the GHS at ∼100 km from the CNSC axis (Sallarès & Charvis 2003). In any case, the melting model can be extrapolated to an intraplate environment by considering the presence of a lithospheric lid limiting the extent of the mantle melting region. The definition and values of all constants and variables used in the model are given in Table 2.

The maximum pressure of melting for adiabatically upwelling mantle corresponds to the point of intersection between the solidus and a given mantle adiabat (Fig. 9c). For dry peridotite, the solidus is defined by the following expression (McKenzie & Bickle 1988):

$$P_0 = (T_0 - 1100)/136 + 4.968 \times 10^{-4} \exp[0.012(T_0 - 1100)], \tag{2}$$

where P_0 is the initial pressure of melting in GPa and T_0 is the temperature at this pressure in °C. The mantle adiabat is defined by its potential temperature, T_p, which can be approximated as follows (McKenzie 1984):

$$T_\mathrm{p} = T_0 - 20P_0. \tag{3}$$

Above the point of intersection between the solidus and the adiabat, the mantle undergoes pressure-release melting. The degree of melting is limited by the heat capacity of mantle particles and the heat of fusion of the matrix as melting proceeds (Forsyth 1993). To first order, the melt fraction is approximated as a linear function, in which a uniform increase in the melt fraction is assumed as the material wells up. In this case, the melt fraction, F, of a parcel of mantle is

$$F = \frac{\partial F}{\partial z}(z_0 - z) = \Gamma(z)(z_0 - z), \tag{4}$$

where z is depth below the crust and $\Gamma\,(z) = \partial F/\partial z$ is the melt productivity, i.e. the fraction of melt per kilometre uplift above the intersection of the solidus and adiabat at depth z_0 (Fig. 9). This parameter is probably the most significant in calculating the amount of melting, and the estimates vary between 10 and 20 per cent GPa^{-1} for dry melting (McKenzie 1984; Langmuir *et al.* 1992), and only ∼1 per cent GPa^{-1} for damp melting (Braun *et al.* 2000). Testing the results obtained for different values of Γ is thus required. The conversion of pressure to depth is done using the expression of lithostatic pressure into the mantle, which is

$$P(z) = g \int_0^z \rho(z)\, dz \approx gz\rho_\mathrm{m}, \tag{5}$$

where g is the acceleration of gravity of the Earth and ρ_m is the average mantle density. The final depth of melting, z_f, is restricted by the thickness of the lithospheric lid, which is composed of newly formed oceanic crust, H, and pre-existing lithosphere or cold oceanic mantle, b, especially in the case that we are far away from the spreading centre (Fig. 9a; Korenaga *et al.* 2002):

$$z_\mathrm{f} = H + b. \tag{6}$$

Following Forsyth (1993), the total volume of melt produced by decompression melting per unit time per unit length of the ridge, $\dot{M}$, can be found by integrating the melt production rate, $\dot{m}$, of an element of mantle over the cross-sectional area in which melting occurs, R (Fig. 9a). We have chosen the simplest triangular melting region, in which the angle of the lithospheric boundary with respect to the horizontal, θ, is 45° (Fig. 9a; Ahern & Turcotte 1979). The melt production rate is the product of the melt productivity, Γ, and the upwelling rate, w, which we define to be the product of the spreading rate, u_0, and the upwelling ratio, χ:

$$\dot{m}(z) = w(z)\frac{\partial F}{\partial z} = u_0\Gamma(z)\chi(z). \tag{7}$$

χ is thus the ratio between mantle upwelling and surface divergence rates. For passive upwelling, it will be $\chi = 1$, with larger values for active upwelling. If we are in an intraplate environment, u_0 corresponds to the plate velocity. For simplicity, we consider that both Γ and χ are only depth-dependent. The melt productivity will be higher in the primary melting zone (i.e. above the dry solidus) than in the damp melting zone, while the upwelling ratio will show the opposite trend (Fig. 9b). Following Ito *et al.* (1999), we assumed passive upwelling above the dry solidus and we tested different values for the maximum active upwelling ratio in the base of the hydrous melting zone (e.g. Maclennan *et al.* 2001).

The crustal thickness, H, is the ratio of the total volume of melt production and the surface divergence rate. Because $\dot{M}$ is given in terms of melt fraction by weight, it is necessary to add a correction factor (ρ_m/ρ_c) to account for the difference between crustal and mantle densities. Considering the model parameters as defined in Fig. 9 and integrating for the mantle melting zone, R, we obtain

$$\begin{aligned} H &= \frac{\rho_m \dot{M}}{\rho_c u_0} = \frac{\rho_m}{\rho_c u_0}\iint_R \dot{m}(x,z)\,dx\,dz \\ &= \frac{\rho_m\left\{3\Gamma_d\left(z_0^2 - z_f^2\right) + \Gamma_w X\Delta z[3z_0(1+\alpha) + \Delta z(2+\alpha)]\right\}}{6\rho_c}, \end{aligned} \tag{8}$$

where Γ_d is the melt productivity in the primary melting zone, Γ_w is the melt productivity in the damp melting region, X is the upwelling ratio at the base of the damp melting region, Δz is the thickness of the damp melting region, and α is the factor of upwelling ratio decay between the base and the top of the damp melting region. Note that z_f can be obtained in a closed form from eqs (6) and (8).

The connection between the mantle melting processes and the seismic velocity of the resultant igneous crust is made using the relationship of Korenaga *et al.* (2002), in which the compressional wave velocities for mantle melts are related to their pressure and degree of melting, $V_p = f(P, F)$, with a multiple linear regression of a number of published melt data (e.g. Kinzler & Grove 1992; Hirose & Kushiro 1993; Kinzler 1997; Korenaga *et al.* 2002). The average degree of melting of all pooled melts, $\bar{F}$, is the integral over the whole melting region of the product of the melt production rate and the degree of melting at a given parcel of mantle, divided by the total melt production (Forsyth 1993):

$$\begin{aligned} \bar{F} &= \frac{1}{\dot{M}}\iint_R F\dot{m}(x,z)\,dx\,dz \\ &= \frac{2\Gamma_d^2\left(z_0^3 - 3z_0z_f^2 + 2z_f^3\right) + \Gamma_w^2 X\Delta z^2[2z_0(1+2\alpha) + \Delta z(1+\alpha)]}{6\Gamma_d\left(z_0^2 - z_f^2\right) + 2\Gamma_w X\Delta z[3z_0(1+\alpha) + \Delta z(2+\alpha)]}. \end{aligned} \tag{9}$$

Finally, the mean depth of melting can be found by integrating the product of the depth and melt production rate over the melting region and dividing by the total melt production (Forsyth 1993):

$$\begin{aligned} \bar{Z} &= \frac{1}{\dot{M}}\iint_R z\dot{m}(x,z)\,dx\,dz \\ &= \frac{4\Gamma_d\left(z_0^3 - z_f^3\right) + \Gamma_w X\Delta z\left[6z_0^2(1+\alpha) + \Delta z^2(3+\alpha) + 4z_0\Delta z(2+\alpha)\right]}{6\Gamma_d\left(z_0^2 - z_f^2\right) + 2\Gamma_w X\Delta z[3z_0(1+\alpha) + \Delta z(2+\alpha)]}. \end{aligned} \tag{10}$$

Similarly to Korenaga *et al.* (2002), we have performed several sample calculations considering different values for the parameters involved. The different panels in Fig. 10 correspond to the so-called H–V_p diagrams, which display the predicted compressional-wave velocity obtained from the multilinear regression of Korenaga *et al.* (2002), using the mean depth and fraction of melting derived from eqs (9) and (10), versus the crustal thickness estimated from eq. (8), as a function of the mantle potential temperature and upwelling ratio. We did several tests using different values for α , Δz, Γ_d and Γ_w, in order to estimate the influence of the different parameters in the calculated diagrams.

6.2 Comparison with velocity models

In order to compare the results predicted by the model with those estimated from wide-angle seismics, we have calculated the long-wavelength crustal structure along the different velocity models obtained at the Carnegie (Fig. 3), Cocos and Malpelo ridges (Sallarès *et al.* 2003). Given that the remaining porosity and alteration of oceanic layer 3 are likely to be small, as suggested by the low-velocity gradient, its average seismic

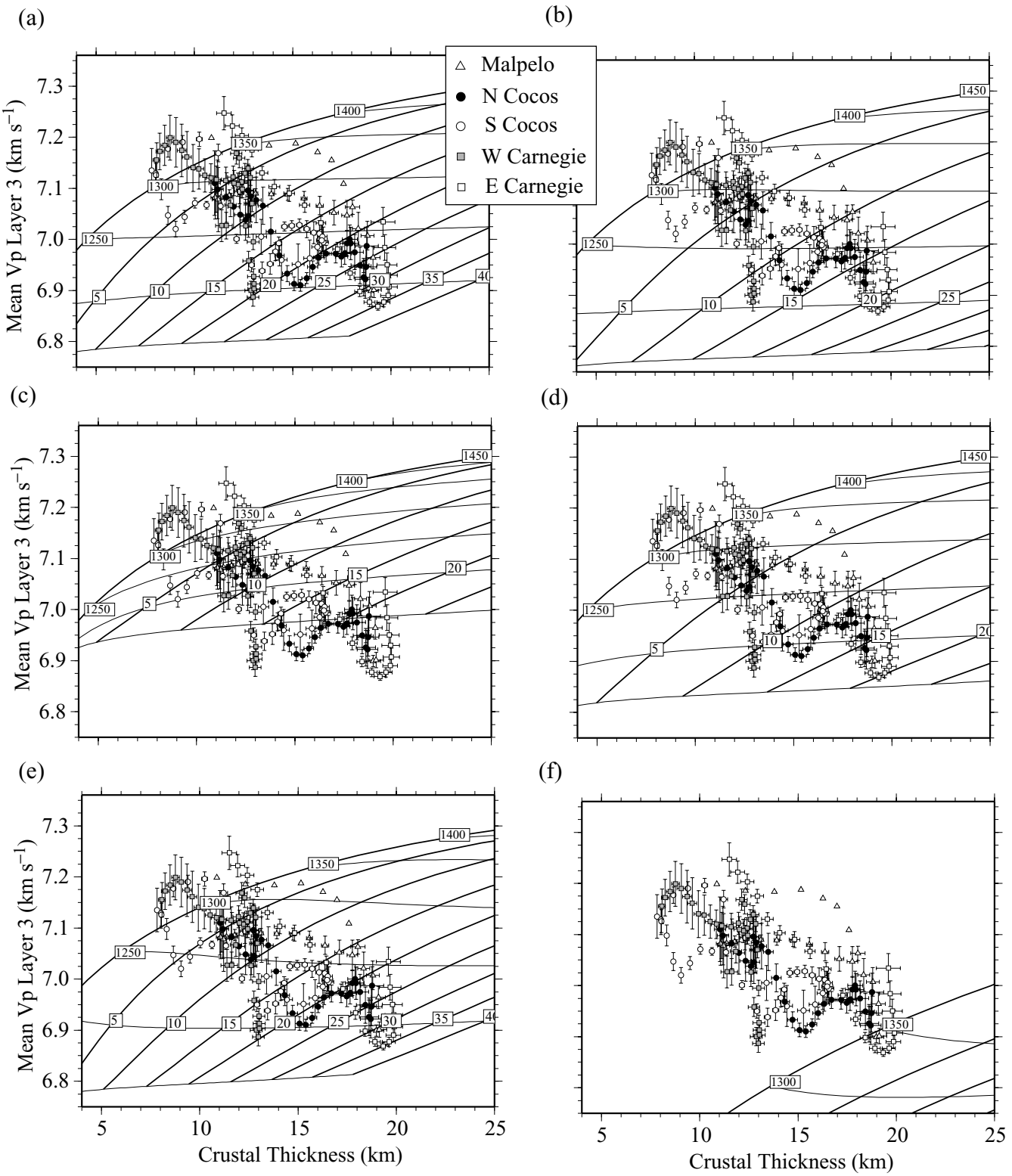

Figure 10. H–V_p diagrams corresponding to different melting parameters. Crustal thickness is plotted versus mean layer 3 velocity. Values are taken from the velocity models estimated along the five profiles indicated in Fig. 1. Southern Cocos (white circles), northern Cocos (solid circles) and Malpelo (triangles) correspond to the models shown in Sallarès *et al.* (2003). Western Carnegie (shaded squares) and eastern Carnegie (white squares) correspond to the models shown in Fig. 3. Thin lines correspond to the mantle potential temperatures and thick lines indicate the upwelling ratio at the base of the mantle melting zone. Melting parameters: (a) $\Gamma_d = 15$ per cent GPa^{-1}, $\Gamma_w = 1$ per cent GPa^{-1}, $\alpha = 0.25$, $\Delta Z = 50$ km, pyrolitic composition; (b) $\Gamma_d = 15$ per cent GPa^{-1}, $\Gamma_w = 1$ per cent GPa^{-1}, $\alpha = 1$, $\Delta Z = 50$ km, pyrolitic composition; (c) $\Gamma_d = 15$ per cent GPa^{-1}, $\Gamma_w = 1$ per cent GPa^{-1}, $\alpha = 0.25$, $\Delta Z = 75$ km, pyrolitic composition; (d) $\Gamma_d = 15$ per cent GPa^{-1}, $\Gamma_w = 2$ per cent GPa^{-1}, $\alpha = 0.25$, $\Delta Z = 50$ km, pyrolitic composition; (e) $\Gamma_d = 20$ per cent GPa^{-1}, $\Gamma_w = 1$ per cent GPa^{-1}, $\alpha = 0.25$, $\Delta Z = 50$ km, pyrolitic composition; (f) same as (e) but with a source composed of 30 per cent MORB and 70 per cent depleted mantle. See details in Section 6.2.

velocity is considered to be a good proxy of the seismic velocity of the igneous crustal rocks (e.g. Kelemen & Holbrook 1995; Korenaga *et al.* 2000). Thus, we have calculated the long-wavelength crustal structure by averaging the layer 3 velocity (V_p) and crustal thickness (H) within a 25-km-wide laterally moving window along the different transects. Uncertainties of model parameters obtained from the Monte Carlo analysis (Fig. 4) are used to assign error bounds to both H and V_p. Because standard H–V_p diagrams are calculated at particular P–T conditions (400 °C, 600 MPa), we corrected V_p from the *in situ* conditions to this reference state, following the approach described in Sallarès *et al.* (2003). The corrected results along all the GVP profiles are represented in the different diagrams obtained using different combinations of the melting parameters, which are shown in Fig. 10. Note that the overall anticorrelation between lower crustal velocity and crustal thickness systematically obtained in the ridges is clearly observed in the H–V_p diagrams.

Fig. 10(a) show the H–V_p diagram obtained using a linear melting function with $\Gamma_d = 15$ per cent GPa^{-1} and $\Gamma_w = 1$ per cent GPa^{-1}. The thickness of the damp melting zone, Δz, is 50 km (e.g. Braun *et al.* 2000), and $\alpha = 0.25$, to be consistent with the 4–5 fold increase of the mantle viscosity between the wet and dry solidus for a water content comparable to the MORB source (Ito *et al.* 1999). This set of parameters defines our reference model. H and V_p are calculated for mantle potential temperatures varying from 1150 to 1450 °C, and an upwelling ratio at the base of the damp melting zone, X, varying from 1 to 40. Note that, in this case, the seismic structure of the thinnest oceanic crust (i.e. that of the normal oceanic basins) is consistent with that expected for a crust generated by passive decompression melting of dry pyrolitic mantle ($X \sim 1$) with a potential temperature of 1300–1350 °C, which is in agreement with the estimates of McKenzie & Bickle (1988). On the contrary, the seismic structure of the thickest crust would require extremely vigorous upwelling ($X \sim 30$–35) of colder than normal mantle ($T_p = 1175$–1200 °C). It seems difficult to imagine a physical process compatible with this result. In the second test (Fig. 10b), we considered a uniform upwelling ratio within the damp melting zone ($\alpha = 1$). The result does not change excessively in terms of estimated potential temperatures and the only difference is that the upwelling ratio would have to be somewhat smaller ($X \sim 20$) to explain the crustal structure of the thickest segments. In the third test (Fig. 10c), we explored the influence of a thicker damp melting zone ($\Delta z = 75$ km). The result is even worse, because the potential temperatures required to explain the crustal thickening must be lower than those estimated for the reference model (Fig. 10a). In the fourth test (Fig. 10d), we considered a higher melt productivity in the damp melting zone ($\Gamma_w = 2$ per cent GPa^{-1}). Again, the result does not change in terms of estimated potential temperatures for the thicker crust ($T_p \sim 1150$ °C) and the maximum upwelling ratio would have to be $X \sim 15$. Finally, we performed another test (Fig. 10e) considering a higher melt productivity within the primary melting zone ($\Gamma_d = 20$ per cent GPa^{-1}), but the only effect that is visible is the lower potential temperatures required to explain the crustal structure of the oceanic basins ($T_p < 1300$ °C). Therefore, the main conclusion of these tests is that it seems difficult to explain the seismic structure of those aseismic ridges considering only deep damp melting coupled with active upwelling. Low mantle potential temperatures would be always required, which is both counter-intuitive and difficult to justify.

6.3 Discussion

A plausible qualitative explanation of the low crustal velocities could be the occurrence of subcrustal fractionation beneath the ridge axis. The loss of high-velocity minerals as material upwells may reduce seismic velocities of the resulting crust in comparison with that resulting from crystallization of a primary, mantle-derived melt. However, it has been shown that the effect of subcrustal fractionation on seismic velocities is only significant for velocities at least 10 per cent higher than those obtained in the lower crust of the Carnegie ridge (Korenaga *et al.* 2002).

Another alternative that must be examined is the presence of compositional anomalies in the mantle source. Isotopic and trace element geochemistry of basalt samples from the Galápagos platform(White *et al.* 1993; Blichert-Toft & White 2001; Harpp & White 2001), the present-day axis of the CNSC (Verma *et al.* 1983; Schilling *et al.* 2003), the Cocos, Carnegie and Malpelo ridges (Hoernle *et al.* 2000; Geldmacher *et al.* 2003; Werner *et al.* 2003), and the Caribbean large igneous province (CLIP; Hauff *et al.* 2000) indicate that the mantle source of the GHS may be internally heterogeneous. The Pb, Hf, Nd and Sr isotopic composition of CNSC lavas suggests the presence of at least two major components for the GHS mantle source, probably corresponding to a recycled mix of oceanic crust—lower-mantle material and to recycled continental-derived material or pelagic sediment (Schilling *et al.* 2003). Basalts from the Galápagos platform show greater scatter in the isotope space, displaying an east facing horseshoe spatial pattern characterized by four main domains (White *et al.* 1993; Harpp & White 2001). The same domains are clearly observed in the Cocos ridge near the subduction zone, indicating the existence of a complex spatial zonation of the GHS magmatism for at least 14 Myr (Hoernle *et al.* 2000). Rocks from the eastern, southern and northern Galápagos domains have enriched signatures reflecting mixtures of depleted MORB source material with different types of altered recycled oceanic crust (Hauff *et al.* 2000). The central Galápagos domain contains the highest ^{3}He/^{4}He ratios, indicating that the source is probably enriched with deep, undegassed mantle material (e.g. Graham *et al.* 1993; Blichert-Toft & White 2001). Likewise, Sr-Nd-Pb isotope and trace element signatures from the CLIP, which is believed to represent the onset of the GHS, are consistent with the derivation from a mixture of a depleted mantle source and recycled oceanic crust (Hauff *et al.* 2000).

Basalts from the GVP also display anomalies in incompatible and major elements with respect to normal MORB. Geochemical data show that lavas from the Galápagos platform have similar Na_2O, lower SiO_2 and slightly higher FeO than do MORB at similar MgO concentration (White *et al.* 1993). In the case that the plume and the asthenosphere have similar major element composition, these observations suggest that the depth of melting is slightly greater to that of melting beneath mid-ocean ridges, but the degree of melting is similar, which is somewhat surprising if the mantle temperatures associated with the hotspot are higher than normal. Fe_8 values (total Fe content as FeO corrected to 8 wt per cent MgO) are highest in the central islands (with values higher than 13 for individual samples) and lowest in the southern and northwestern ones, suggesting deeper melting beneath the central part of the platform (Geist 1992; White *et al.* 1993).

In the CNSC, lavas sampled away from the zone of maximal GHS influence show Fe_8 values higher than 11 (e.g. at the 87°–88° W segment), which are relatively elevated for their axial depth (∼2200 meters below seafloor; Christie *et al.* 2005). However, the correlations of Fe_8 and Na_8 (total Na content as Na_2O corrected to 8 wt per cent MgO) with axial depth and crustal thickness along the GHS-influenced segment of the CNSC are different to those of the global MORB array, the thickest crust and shallowest axial depth being characterized by the lowest Fe_8 and the highest Na_8 (e.g. Klein & Langmuir 1987; Langmuir *et al.* 1992; Christie *et al.* in press; Cushman *et al.* 2005). The Fe_8 decrease and Na_8 increase along the CNSC as we approach the GHS contradict apparently with the presence of a hotter mantle, as increasing potential temperature would have to lead to deeper melting and higher FeO, as well as to a higher extent of melting and lower Na_2O, at a given MgO. Asimow & Langmuir (2003) explained the apparent discrepancy between mantle temperature and Fe_8 in terms of water addition to the mantle source. They showed that one of the dominant effects of water is the suppression of plagioclase crystallization, which leads to lower FeO contents in fractionated liquids compared with anhydrous melting. Likewise, Cushman *et al.* (2005) showed that hydrous melting may also account for the observed correlation between Na_8 and crustal thickness, suggesting that melting of a deep, hydrous root is the dominant process to account for the geophysical and geochemical variations along the western CNSC. Damp melting alone does not explain, however, the higher Fe_8 values observed in the volcanoes of the central Galápagos platform as compared with the southern (and northern) ones (Geist 1992; White *et al.* 1993), and the high Fe_8 values of the easternmost CNSC segments (Christie *et al.* in press). Normally, one would expect to have low Fe_8 values also at the zone of maximal hotspot influence (beneath the platform). However, this is not the case, which may indicate either (i) the influence of deep damp melting is not significant beneath the platform, or (ii) the mantle melting source is somehow enriched in iron.

The model described in Section 6.1 is only valid for mantle compositions similar to pyrolite, because the relationship between seismic velocity and melting parameters used in this study (Korenaga *et al.* 2002) was estimated for this model composition only. The uniform composition of most ocean peridotites is well explained by melting of a pyrolitic mantle and thus the assumption of a uniform pyrolitic mantle is probably justified in most cases. Nevertheless, the presence of major element heterogeneities in the mantle source has been suggested in some special cases, namely the generation of large igneous provinces and flood basalts (e.g. Campbell 1998). In particular, Korenaga & Kelemen (2000) suggested that most of the magmatism of the North Atlantic igneous province may be owing to a relatively Fe-rich mantle source (Mg # ∼0.87) with respect to the normal MORB source (Mg # ∼ 0.90), and they indicated that such a source could be a mixture of depleted upper mantle and ancient, recycled oceanic crust, which is similar to that proposed for the GVP and the CLIP based on isotopic and trace element geochemistry (Hauff *et al.* 2000; Hoernle *et al.* 2000; Harpp & White 2001; Schilling *et al.* 2003). Based on the results of an experimental study of the phase and melting relations of homogeneous basalt and peridotite mixtures, Yaxley (2000) showed that the lower solidus and compressed solidus–liquidus temperature interval of material containing a few tens of per cent basalt in peridotite may combine during mantle upwelling to substantially enhance melt production. Hence, he suggested that mixtures of recycled oceanic crust and peridotite in mantle plumes may provide a plausible source for extra melting (as previously suggested by Cordery *et al.* 1997), and that the resulting primary melting liquids would have to show higher than normal Fe/Mg values (lower Mg #).

However, too few melting experiments with source compositions different from pyrolite exist to develop a quantitative model including the effect of source heterogeneities. Korenaga *et al.* (2002) performed a preliminary attempt to illustrate the potential effect of a major element heterogeneity such as that described for the North Atlantic province. They considered a hypothetical source composed of 70 per cent depleted pyrolitic mantle (Kinzler 1997) and 30 per cent MORB (Hofmann 1988; Mg # ∼ 0.86), calculated isobaric batch melts, and derived a relationship between the norm-based velocity (see definition in Korenaga *et al.* 2002) and the melting parameters. Similarly, we have performed a final test with our model using the same relationship combined with a higher melt productivity in the primary melting zone (20 per cent GPa^{-1}) and a 50 °C lower temperature in the solidus with respect to normal pyrolite in order to reflect the Fe enrichment (Fig. 10f). These modelling results indicate that the seismic structure of the thickest crustal segments can be more easily explained by passive to moderately active upwelling of a normal temperature but fertile mantle source rather than by that of a hot and homogeneus pyrolitic mantle, even if vigorous upwelling of a hydrous mantle root is included in the model. This is in agreement with that previously suggested by Sallarès *et al.* (2003) based on the velocity–thickness anticorrelation obtained in Cocos and Malpelo.

Melting of recycled subducted oceanic crust in the mantle source could thus explain qualitatively the observed isotope and trace element patterns, as well as the crustal thickening and the anticorrelation between crustal thickness and layer 3 velocity of the aseismic ridges, without the need to consider anomalously high mantle temperatures. As we stated above, the isotopic composition of CNSC, GVP and CLIP lavas seems to indicate the presence of a component corresponding to a recycled mix of oceanic crust and lower-mantle material (Hauff *et al.* 2000; Hoernle *et al.* 2000; Schilling *et al.* 2003), which could potentially lead to deeper melting, enhanced melt production (i.e. a thicker crust) and relatively high FeO values for a given MgO (e.g. Yaxley 2000). This is generally consistent with the FeO trends observed in the Galápagos archipelago (White *et al.* 1993), but we suggest that the occurrence of deep damp melting may probably smooth or even counterbalance this tendency, especially along the CNSC. The Sm-Nd and U-Pb isotope systematics indicate that the CLIP source components were separated from a common depleted MORB source <500 Myr before CLIP formation (90–100 Ma), which has been interpreted to reflect the recycling age of the oceanic lithosphere (Hauff *et al.* 2000). These authors propose large volume contamination of the upper mantle with young recycled oceanic lithosphere by means of multiple mid-Cretaceous starting plume heads (e.g. Hanan & Graham 1996) as a plausible origin for the mantle source heterogeneity of the GHS. In addition, a contribution of extra melting from a deep and hydrous root is probably needed to account for the high Na_8 and low Fe_8 values along the most GHS-affected segment of the CNSC (Asimow & Langmuir 2003; Cushman *et al.* 2005). The relative significance of fertile versus damp melting is however difficult to quantify, owing to the lack of available mantle melting experiments using model compositions different from pyrolitic.

One aspect difficult to reconcile with the hypothesis of basalt addition to the mantle source prior to melting as the origin of the GVP concerns the upwelling mechanism of the denser mantle heterogeneity in the absence of a thermal plume. It is clear that present upwelling beneath the Galápagos archipelago can not be simply a passive response to seafloor spreading. The Galápagos platform is too far away from the CNSC, so it is necessary to have a source of active upwelling to explain the current hotspot volcanism. If we rule out the presence of a thermal anomaly (which, if present, must be weak, just a few tens of degrees according to Cushman *et al.* 2005), mantle upwelling must be associated either with compositional buoyancy or with the presence of any other type of sublithospheric convection. Subducted oceanic crust is denser than normal pyrolitic mantle above the bottom of the mantle transition zone (Ringwood & Irifune 1988), so it will tend to lie at this level of neutral buoyancy unless it is sent back to the surface by a rising stream. A plausible mechanism that has been shown to be capable of bringing up dense fertile mantle without a thermal anomaly is sublithospheric convection driven by surface cooling (Korenaga 2004). This model has been proposed to explain the origin of continental breakup magmatism of the North Atlantic volcanic province, but it is apparently more difficult to associate the GHS volcanism to a similar process. An alternative that must be examined in order to explain active upwelling is the effect of water content on mantle buoyancy. It has been shown that the presence of water in the mantle source reduces substantially mantle viscosity and enhances mantle flow, increasing, in turn, the mantle upwelling rates (Ito *et al.* 1999), but the direct effect of water content on density variations and buoyancy is not constrained so far.

7 SUMMARY AND CONCLUSIONS

We have estimated the crustal structure of the Carnegie ridge from refraction/reflection traveltime tomography along two wide-angle seismic transects located over ∼20 and ∼11.5 Myr old seafloor over the Nazca Plate at the GVP. The crust shows a typical oceanic structure, composed of an upper layer characterized by striking velocity gradients (i.e. the oceanic layer 2) and a lower layer showing much more uniform velocity (i.e. the layer 3). However, the crust is much thicker than normal. In profile 1 (Fig. 1), maximum crustal thickness is around 13 km, thus it is twice the thickness of normal oceanic crust, while in profile 2 it is around 19 km. In both profiles, layer 2 thickness is quite uniform (3–4 km) regardless of total crustal thickness variations, indicating that the excess of melting provided by the GHS is mainly accommodated by layer 3. The velocity structure obtained across the Carnegie ridge is almost identical to that previously estimated at the conjugate profiles of the Carnegie ridge ones over the Cocos and Malpelo ridges, and in another one across the Cocos ridge over ∼15 Myr old seafloor (Sallarès *et al.* 2003). This suggests that all the volcanic edifices of the GVP are probably the product of a single, long-lasting mantle melting anomaly, in conjunction with a regular process of ridge edification, which has been active for at least the last 20 Myr. A recent study based on all these data has shown that the crustal thickness variations at the different GVP aseismic ridge segments are the effect of temporal variations in the relative location between the CNSC and the GHS, and not that of temporal GHS intensity variations, indicating that the anomaly is additionally a stable and unvarying mantle feature (Sallarès & Charvis 2003). The estimated crustal velocity models along the different transects are also consistent with gravity and bathymetry data. The velocity-derived density models show that Carnegie, Cocos and Malpelo have uniform normal upper-mantle densities, indicating that GVP aseismic ridges are isostatically compensated at the base of the crust. Therefore, there is not compelling evidence for the presence of upper-mantle density anomalies, indicating that such mantle anomalies, if present when the ridges were originated, are not significant for ages older than 10 Myr.

A remarkable feature that is systematically observed in all the aseismic ridges is the overall anticorrelation between layer 3 velocities (and densities) and total crustal thickness. A 2-D steady-state mantle melting model based on that of Korenaga *et al.* (2002) is developed and used to illustrate that it is very difficult to account for the seismic structure of the GVP ridges if it is assumed that the source of the GHS is a thermal anomaly, even if vigorous mantle upwelling coupled with deep damp melting is included in the model. It seems easier to account for the estimated crustal structure if a more drastic, major element heterogeneity, is also considered in the melting model. Based on these results, we suggest that the primary source of the GHS is a compositional heterogeneity, which may represent a mixture of depleted mantle and recycled oceanic crust (e.g. Yaxley 2000). Such a mantle source explains well the isotope and trace element patterns showed by GVP and CLIP basalts (Schilling *et al.* 1982; Hauff *et al.* 2000; Schilling *et al.* 2003). Additional deep and hydrous mantle melting is probably needed to account for the high Na_8 and low Fe_8 observed in the most GHS-affected segment the CNSC (Detrick *et al.* 2002; Asimow & Langmuir 2003; Cushman *et al.* 2005). Mantle melting experiments for mantle source compositions different from pyrolitic are though required to quantify the relative significance of fertile versus damp melting to account for the origin of the GVP.

ACKNOWLEDGMENTS

The SALIERI-2001 experiment was funded by the German Ministry of Education, Research, Science and Technology (BMBF) under project no. 03G0159A. The French scientific party was supported by IRD, Institut National des Sciences de l'Univers (INSU) and French Research Institute for Exploitation of the Sea (IFREMER) through ship time exchange. VS was financially supported by a grant from the Marie Curie Fellowship EU programme, contract no. HPRI–CT–1999–00037, during the time the work was conducted. We thank the Associate Editor, Jean Francheteau, as well as the reviewers Juan Pablo Canales and Jun Korenaga, for their constructive reviews, which helped to improve substantially the original version of the manuscript. We are also indebted to H. Andersen, master of the R/V Sonne, and to the crew of the vessel for their professional support and the good working atmosphere during the cruise. This is Géosciences Azur contribution no. 640.

REFERENCES

Ahern, J.L. & Turcotte, D.L., 1979. Magma migration beneath an oceanic ridge, *Earth planet. Sci. Lett.,* **45,** 115–122.

Anderson, R.N., McKenzie, D. & Sclater, J.G., 1973. Gravity, bathymetry and convection in the Earth, *Earth planet. Sci. Lett.,* **18,** 391–407.

Asimow, P.D. & Langmuir, C.H., 2003. The importance of water to oceanic mantle melting regimes, *Nature*, **421,** 815–820.

Barckhausen, U., Ranero, C.R., von Huene, R., Cande, S.C. & Roeser, H.A., 2001. Revised tectonic boundaries in the Cocos plate off Costa Rica: Implications for the segmentation of the convergent margin and for plate tectonic models, *J. geophys. Res.,* **106,** 19 207–19 220.

Barton, A.J. & White, R.S., 1997. Crustal structure of the Edoras Bank continental margin and mantle thermal anomalies beneath the North Atlantic, *J. geophys. Res.,* **102,** 3109–3129.

Bijwaard, H. & Spakman, W., 1999. Tomographic evidence for a narrow whole mantle plume below Iceland, *Earth planet. Sci. Lett.*, **166,** 121–126.

Blichert-Toft, J. & White, W.M., 2001. Hf isotope geochemistry of the Galápagos Islands, *Geochem., Geophys., Geosys.,* **2,** doi: 10.1029/1999GC000138.

Bonatti, E., 1990. Not so hot 'hot spots' in the oceanic mantle, *Science,* **250**(4977), 107–111.

Boutilier, R.R. & Keen, C.E., 1999. Small-scale convection and divergent plate boundaries, *J. geophys. Res.,* **104,** 7389–7403.

Braun, M.G., Hirth, G. & Parmentier, E.M., 2000. The effects of deep damp melting on mantle flow and melt generation beneath mid-oceanic ridges, *Earth planet. Sci. Lett.,* **176,** 339–356.

Campbell, I.H., 1998. The mantle's chemical structure: insights from the melting products of mantle plumes, in *The Earth's mantle: composition, structure and evolution,* pp. 259–310. ed. Jackson, I., Cambridge University Press, Cambridge.

Canales, J.P., Ito, G., Detrick, R.S. & Sinton, J., 2002. Crustal thickness along the western Galápagos Spreading Center and compensation of the Galápagos Swell, *Earth planet. Sci. Lett.,* **203,** 311–327.

Carlson, R.L. & Herrick, C.N., 1990. Densities and porosities in the oceanic crust and their variations with depth and age, *J. geophys. Res.,* **95,** 9153–9170.

Charvis, P. & Operto, S., 1999. Structure of the Cretaceous Kerguelen Volcanic Province (southern Indian Ocean) from wide-angle seismic data, *J. Geodyn.,* **28,** 51–71.

Charvis, P., Recq, M., Operto, S. & Brefort, D., 1995. Deep structure of the northern Kerguelen Plateau and hotspot-related activity, *Geophys. J. Int.,* **122,** 899–924.

Christie, D., Werner, R., Hauff, F., Hoernle, K. & Hanan, B., 2005. Morphological and geochemical variations along the eastern Galápagos Spreading Center, *Geochem., Geophys., Geosys.*, in press.

Cochran, J.R. & Talwani, M., 1977. Free-air gravity anomalies in the world's oceans and their relationship to residual elevation, *Geophys. J. R. astr. Soc.,* **50,** 495–552.

Coffin, M.F. & Eldholm, O., 1994. Large Igneous Provinces: Crustal structure, dimensions & external consequences, *Rev. Geophys.,* **32,** 1–36.

Cordery, M.J., Davies, G.F. & Campbell, I.H., 1997. Genesis of flood basalts from eclogite-bearing mantle plumes, *J. geophys. Res.,* **102,** 20 179–20 197.

Courtillot, V., Davaille, A., Besse, J. & Stock, J., 2003. Three distinct types of hotspots in the Earth's mantle, *Earth planet. Sci. Lett.,* **205,** 295–308.

Courtney, R.C. & White, R.S., 1986. Anomalous heat flow and geoid across the Cape Verde Rise: evidence for dynamic support from a thermal plume in the mantle, *Geophys. J. R. astr. Soc.,* **87,** 815–867.

Cushman, B., Sinton, J., Ito, G. & Dixon, J.E., 2005. Glass compositions, plume-ridge interaction, and hydrous melting along the Galápagos Spreading Center, 90.5°W to 98°W, *Geochem., Geophys., Geosys.,* in press.

Darbyshire, F.A., White, R.S. & Priestley, K.F., 2000. Structure of the crust and uppermost mantle of Iceland from a combined seismic and gravity study, *Earth planet. Sci. Lett.,* **181,** 409–428.

DeMets, C., Gordon, R.G., Argus, D.F. & Stein, S., 1990. Current plate motions, *Geophys. J. Int.,* **101,** 425–478.

Detrick, R.S., Collins, J., Stephen, R. & Swift, S., 1994. In situ evidence for the nature of the Layer 2/3 boundary in oceanic crust, *Nature,* **370,** 288–290.

Detrick, R.S. *et al.*, 2002. Correlated geophysical, geochemical & volcanological manifestations of plume-ridge interaction along the Galápagos Spreading Center, *Geochem., Geophys., Geosyst.,* **3,** doi: 10.1029/2002GC000350.

Escartín, J., Cannat, M., Pouliquen, G. & Rabain, A., 2001. Crustal thickness of V-shaped ridges south of the Azores: Interaction of the Mid-Atlantic Ridge (36°–39°N) and the Azores hot spot, *J. geophys. Res.,* **106,** 21 719–21 734.

Flueh, E.R., Bialas, J., Charvis, P. & the Salieri Scientific Party, 2001. *Cruise report SO159 SALIERI,* GEOMAR, Kiel.

Forsyth, D.W., 1993. Crustal thickness and the average depth and degree of melting in fractional melting models of passive flow beneath mid-ocean ridges, *J. geophys. Res.,* **98,** 16 073–16 079.

Foulger, G.R. *et al.*, 2001. Seismic tomography shows that upwelling beneath Iceland is confined to the upper mantle, *Geophys. J. Int.*, **146,** 504–530.

Freymueller, J.T., Kellogg, J.N. & Vega, V., 1993. Plate motions in the North-Andean region, *J. geophys. Res.,* **98,** 21 853–21 863.

Geist, D.J., 1992. An appraisal of melting processes and the Galápagos hotspot: Major and trace element evidence, *J. Volc. Geotherm. Res.,* **52,** 65–82.

Geldmacher, J., Hanan, B., Blichert-Toft, J., Harpp, K.S., Hoernle, K., Hauff, F., Werner, R. & Kerr, A., 2003. Hafnium isotopic variations in volcanic rocks from the Caribbean Large Igneous Province and Galápagos hotspot tracks, *Geochem. Geophys. Geosyst.,* **3,** doi:10.1029/2002GC000477.

Graham, D.W., Christie, D.M., Harpp, K.S. & Lupton, J.E., 1993. Mantle plume helium in submarine basalts from the Galápagos platform, *Science,* **262,** 2023–2026.

Graindorge, D., Calahorrano, A., Charvis, Ph., Collot, J.-Y. & Bethoux, N., 2004. Deep structures of the Ecuador convergent margin and the Carnegie Ridge, possible consequence on great earthquakes recurrence interval, *Geophys. Res. Lett.,* **31,** L04603, doi:10.1029/2003GL018803.

Grevemeyer, I., Flueh, E.R., Reichert, C., Bialas, J., Klaeschen, D. & Kopp, C., 2001. Crustal architecture and deep structure of the Ninetyeast Ridge hotspot trail from active source ocean bottom seismology, *Geophys. J. Int.,* **144,** 1–22.

Hamilton, E.L., 1978. Sound velocity–density relations in seafloor sediments and rocks, *J. acoust. Soc. Am.,* **63,** 366–377.

Hanan, B.B. & Graham, D.W., 1996. Lead and helium isotope evidence from oceanic basalts for a common deep source of mantle plumes, *Science,* **272,** 991–995.

Hardy, N.C., 1991. Tectonic evolution of the easternmost Panama Basin: Some new data and inferences, *J. S. Am. Earth Sci.,* **4**(3), 261–269.

Harpp, K.S. & White, W.M., 2001. Tracing a mantle plume: Isotopic and trace element variations of Galápagos seamounts, *Geochem., Geophys., Geosyst.,* **2,** paper 2000GC000137.

Hauff, F., Hoernle, K., Tilton, G., Graham, D.W. & Kerr, A.C., 2000. Large volume recycling of oceanic lithosphere over short time scales: geochemical constraints from the Caribbean Large Igneous Province, *Earth planet. Sci. Lett.,* **174,** 247–263.

Hauri, E.H., 1996. Major element variability in the Hawaiian mantle plume, *Nature,* **382,** 415–419.

Hey, R., 1977. Tectonic evolution of the Cocos–Nazca spreading center, *Geol. soc. Am. Bull.,* **88,** 1404–1420.

Hirose, K. & Kushiro, I., 1993. Partial melting of dry peridotites at high pressures: Determination of composition of melts segregated from peridotite using aggregates of diamond, *Earth planet. Sci. Lett.,* **114,** 477–489.

Hirth, G. & Kohlstedt, D.L., 1996. Water in the oceanic upper mantle: implications for rheology, melt extraction and the evolution of the lithosphere, *Earth planet. Sci. Lett.,* **144,** 93–108.

Hoernle, K.A., Werner, R., Phipps-Morgan, J., Bryce, J. & Mrazek, J., 2000. Existence of complex spatial zonation in the Galápagos plume for at least 14.5 Ma, *Geology,* **28,** 435–438.

Hofmann, A.W., 1988. Chemical differentiation of the Earth: the relationship between mantle, continental crust & oceanic crust, *Earth planet. Sci. Lett.,* **90,** 297–314.

Hooft, E.E.E., Toomey, D.R. & Solomon, S.C., 2003. Anomalously thin transition zone beneath the Galápagos hotspot, *Earth planet. Sci. Lett.,* **216,** 55–64.

Ito, G. & Lin, J., 1995. Mantle temperature anomalies along the past and paleoaxes of the Galápagos spreading center as inferred from gravity analyses, *J. geophys. Res.,* **100,** 3733–3745.

Ito, G., Lin, J. & Gable, C.W., 1996. Dynamics of mantle flow and melting at a ridge-centered hotspot: Iceland and the Mid-Atlantic Ridge, *Earth planet. Sci. Lett.,* **144,** 53–74.

Ito, G., Lin, J. & Gable, C.W., 1997. Interaction of mantle plumes and migrating mid-ocean ridges: Implications for the Galápagos plume-ridge system, *J. geophys. Res.,* **102,** 15 403–15 417.

Ito, G., Shen, Y., Hirth, G. & Wolfe, C.J., 1999. Mantle flow, melting and dehydration of the Iceland mantle plume, *Earth planet. Sci. Lett.,* **165,** 81–96.

Kelemen, P.B. & Holbrook, W.S., 1995. Origin of thick, high-velocity igneous crust along the U.S. East Coast margin, *J. geophys. Res.,* **100,** 10 077–10 094.

Kinzler, R.J., 1997. Melting of mantle peridotite at pressures approaching the spinel to garnet transition: Application to mid-ocean ridge basalt petrogenesis, *J. geophys. Res.,* **102,** 852–874.

Kinzler, R.J. & Grove, T.L., 1992. Primary magmas of mid-ocean ridge basalts, 2, applications, *J. geophys. Res.,* **97,** 6907–6926.

Klein, E.M. & Langmuir, C.H., 1987. Global correlations of ocean ridge basalt chemistry with axial depth and crustal thickness, *J. geophys. Res.,* **92,** 8089–8115.

Korenaga, J., 2004. Mantle mixing and continental breakup magmatism, *Earth planet. Sci. Lett.,* **218,** 463–473.

Korenaga, J. & Jordan, T. H., 2002. On the state of sublithospheric upper mantle beneath a supercontinent, *Geophys. J. Int.,* **149,** 179–189.

Korenaga, J. & Kelemen, P.B., 2000. Major element heterogeneity in the mantle source of the North Atlantic igneous province, *Earth planet. Sci. Lett.,* **184,** 251–268.

Korenaga, J., Holbrook, W.S., Kent, G.M., Kelemen, P.B., Detrick, R.S., Larsen, H.-C., Hopper, J.R. & Dahl-Jensen, T., 2000. Crustal structure of the southeast Greenland margin from joint refraction and reflection seismic tomography, *J. geophys. Res.,* **105,** 21 591–21 614.

Korenaga, J., Holbrook, W.S., Detrick, R.S. & Kelemen, P.B., 2001. Gravity anomalies and crustal structure at the southeast Greenland margin, *J. geophys. Res.,* **106,** 8853–8870.

Korenaga, J., Kelemen, P.B. & Holbrook, W.S., 2002. Methods for resolving the origin of large igneous provinces from crustal seismology, *J. geophys. Res.,* **107**(B9), 2178, doi:10.1029/2001JB001030.

Langmuir, C.H., Klein, E.M. & Plank, T., 1992. Petrological systematics of mid-ocean ridge basalts: Constraints on melt generation beneath mid-oceanic ridges, *Geophys. Monogr.,* **71,** 183–280.

Laske, G., Phipps Morgan, J. & Orcutt, J.A., 1999. First results from the Hawaiian SWELL Pilot Experiment, *Geophys. Res. Lett.,* **26,** 3397–3400.

Lonsdale, P. & Klitgord, K.D., 1978. Structure and tectonic history of the eastern Panama Basin, *Geol. soc. Am. Bull.,* **89,** 981–999.

Maclennan, J., McKenzie, D. & Gronvold, K., 2001. Plume-driven upwelling under central Iceland, *Earth planet. Sci. Lett.***194,** 67–82.

McKenzie, D., 1984. The generation and compaction of partially molten rock, *J. Petrol.,* **25,** 713–765.

McKenzie, D. & Bickle, M.J., 1988. The volume and composition of melt generated by extension of the lithosphere, *J. Petrol.,* **29,** 625–679.

McNutt, M.K. & Bonneville, A., 2000. A shallow, chemical origin, for the Marquesas swell, *Geochem., Geophys., Geosys.,* **1,** paper no. 1999GC000028.

Matarese, J.R., 1993. Nonlinear traveltime tomography, *PhD thesis*, Mass. Inst. of Technol., Cambridge.

Montelli, R., Nolet, G., Dahlen, F.A., Masters, G. & Engdahl, E.R., 2004. Finite-frequency Tomography reveals a variety of plumes in the mantle, *Science,* **303,** 5656, 338–343.

Morgan, W.J., 1971. Convection plumes in the lower mantle, *Nature,* **230,** 42–43.

Mueller, R.D., Roest, W.R., Royer, J.-Y., Gahagan, L.M. & Sclater, J.G., 1996. *A digital age map of the ocean floor,* SIO Reference Series 93–30, Scripps Institution of Oceanography, La Jolla, CA, USA.

Mutter, C.Z. & Mutter, J.C., 1993. Variations in thickness of Layer 3 dominate oceanic crustal structure, *Earth planet. Sci. Lett.,* **117,** 295–317.

Oxburgh, E.R. & Parmentier, E.M., 1977. Compositional and density stratification in oceanic lithosphere—causes and consequences, *J. geol. Soc. Lond.,* **133,** 343–355.

Parker, R.L., 1972. The rapid calculation of potential anomalies, *Geophys. J. R. astr. Soc.,* **31,** 447–455.

Parsons, B. & Sclater, J.G., 1977. An analysis of the variation of ocean floor bathymetry and heat fow with age, *J. geophys. Res.,* **82,** 803–826.

Phipps Morgan, J., Morgan, W.J. & Price, E., 1995. Hotspot melting generates both hotspot volcanism and a hotspot swell?, *J. geophys. Res.,* **100,** 8045–8062.

Plank, T. & Langmuir, C.H., 1992. Effects of melting regime on the composition of the oceanic crust, *J. geophys. Res.,* **97,** 19 749–19 770.

Plank, T., Spiegelman, M., Langmuir, C.H. & Forsyth, D.H., 1995. The meaning of 'mean F': Clarifying the mean extent of melting at ocean ridges, *J. geophys. Res.,* **100,** 15 045–15 052.

Ringwood, A.E. & Irifune, T., 1988. Nature of the 650-km seismic discontinuity—implications for mantle dynamics and differentiation, *Nature,* **331,** 131–136.

Ritsema, J. & Allen, R.M., 2003. The elusive mantle plume, *Earth planet. Sci. Lett.,* **207,** 1–12.

Sallarès, V. & Charvis, Ph., 2003. Crustal thickness constraints on the geodynamic evolution of the Galápagos volcanic province, *Earth planet. Sci. Lett.,* **214**(3–4), 545–559.

Sallarès, V., Charvis, Ph., Flueh, E.R. & Bialas, J., 2003. Seismic structure of Cocos and Malpelo ridges and implications for hotspot-ridge interaction, *J. geophys. Res.,* **108,** 2564, doi: 10.1029/2003JB002431.

Sandwell, D.T. & Smith, W.H.F., 1997. Marine gravity anomaly from Geosat and ERS-1 satellite altimetry, *J. geophys. Res.,* **102,** 10 039–10 054.

Schilling, J.-G., 1985. Upper mantle heterogeneities and dynamics, *Nature,* **314,** 62–67.

Schilling, J.-G., 1991. Fluxes and excess temperatures of mantle plumes inferred from their interaction with migrating mid-oceanic ridges, *Nature,* **352,** 397–403.

Schilling, J.-G., Kingsley, H. & Devine, J.D., 1982. Galápagos hotspot–spreading center system, 1, Spatial petrological and geochemical variations (83°W–101°W), *J. geophys. Res.,* **87,** 5593–5610.

Schilling, J.-G., Zajac, M., Evans, R., Johnson, T., White, W., Devine, J.D. & Kingsley, R., 1983. Petrological and geochemical variations along the Mid-Atlantic ridge from 29°N to 73°N, *Am. J. Sci.,* **283,** 510–586.

Schilling, J.-G., Fontignie, D., Blichert-Toft, J., Kingsley, R. & Tomza, U., 2003. Pb-Hf-Nd-Sr isotope variations along the Galápagos Spreading Center (101°-83°W): Constraints on the dispersal of the Galápagos mantle plume, *Geochem. Geophys. Geosyst.,* **4,** doi:10.1029/2002GC000495.

Sleep, N.H., 1990. Hotspots and mantle plumes—some phenomenology, *J. geophys. Res.,* **95,** 6715–6736.

Tarantola, A., 1987. *Inverse problem theory: Methods for data fitting and model parameter estimation,* Elsevier Science, New York, p. 613.

Toomey, D.R. & Foulger, G.R., 1989. Tomographic inversion of local earthquake data from the Hengill-Grensdalur central volcano complex, Iceland, *J. geophys. Res.,* **94,** 17 497–17 510.

Toomey, D.R., Hooft, E.E. & Detrick, R.S., 2001. Crustal thickness variations and internal structure of the Galápagos Archipiélago, *EOS, Trans. Am. geophys. Un.,* **82**(47), Fall Meet. Suppl., Abstr. T42B-0939.

Trenkamp, R., Kellogg, J.N., Freymueller, J.T. & Mora, H.P., 2002. Wide plate margin deformation, southern Central America and northwestern South America, CASA GPS observations, *J. S. Am. Earth Sci.,* **15,** 157–171.

Trummer, I., Flueh, E.R. & the PAGANINI Working Group, 2002. Seismic constraints on the crustal structure of Cocos Ridge off the coast of Costa Rica, *Jahrbuch der Geologishen und Paläontologische Abhandlungden* **225**(1), 25–37.

Verma, S.P., Schilling, J.-G. & Waggoner, D.G., 1983. Neodyum isotopic evidence for Galápagos hotspot-spreading centre system evolution, *Nature,* **306,** 654–657.

Walther, C., 2002. Crustal structure of the Cocos Ridge northeast of Cocos Island, Panama Basin, 2002, *Geophys. Res. Lett.,* **29**(20), 1986, doi:10.1029/2001GL014267.

Walther, C., 2003. The crustal structure of the Cocos ridge off Costa Rica, *J. geophys. Res.,* **108,** doi:10.1029/2001JB000888.

Watson, S. & McKenzie, D., 1991. Melt generation by plumes: a study of Hawaiian volcanism, *J. Petrol.,* **32,** 501–537.

Werner, R., Hoernle, K., Barckhausen, U. & Hauff, F., 2003. Geodynamic evolution of the Galápagos hostspot system (Central East Pacific) over the past 20 Myr: Constraints from morphology, geochemistry and magnetic anomalies, *Geochem. Geophys. Geosyst.,* **3,** doi:10.1029/2003GC00576.

White, R.S. & McKenzie, D., 1989. Magmatism at rift zones: The generation of volcanic continental margins and flood basalts, *J. geophys. Res.,* **94,** 7685–7794.

White, R.S. & McKenzie, D., 1995. Mantle plumes and flood basalts, *J. geophys. Res.,* **100,** 17 543–17 585.

White, R.S., McKenzie, D. & O'Nions, R.K., 1992. Oceanic crustal thickness from seismic measurements and Rare Earth Element inversions, *J. geophys. Res.,* **97,** 19 683–19 715.

White, W.M., McBirney, A.R. & Duncan, R.A., 1993. Petrology and geochemistry of the Galápagos islands: Portrait of a pathological mantle plume, *J. geophys. Res.,* **98**(11), 19 533–19 563.

Wilson, D.S. & Hey, R. N., 1995. History of rift propagation and magnetization intensity for the Cocs-Nazca spreading center, *J. geophys. Res.,* **100,** 10 041–10 056.

Wilson, J.T., 1963. A possible origin of the Hawaiian Islands, *Can. J. Phys.,* **41,** 863–870.

Wolfe, C.J., Bjarnason, I.T., VanDecar, J.C. & Solomon, S.C., 1996. Seismic structure of the Iceland mantle plume, *Nature,* **385,** 245–247.

Wolfe, C.J., Bjarnason, I.T., VanDecar, J.C. & Solomon, S.C., 2002. Assessing the depth resolution of tomographic models of upper mantle structure beneath Iceland, *Geophys. Res. Lett.,* **29**(2), 1015, 10.1029/2001GL013657.

Yaxley, G.M., 2000. Experimental study of the phase and melting relations of homogeneous basalt + peridotite mixtures and implications for the petrogenesis of flood basalts, *Contrib. Mineral. Petr.,* **139,** 326–338.